High-Resolution peripheral Quantitative Computed Tomography Based Finite Element Modelling of Distal Radius Strength: Assessing Effect of Heterogeneous Material Properties and Scan Site

A Thesis Submitted to the College of
Graduate and Postdoctoral Studies
in Partial Fulfillment of the Requirements
for the Degree of Master of Science
in the Division of Biomedical Engineering
University of Saskatchewan
Saskatoon

By
Seyedmahdi Hosseinitabatabaei

PERMISSION TO USE

In presenting this thesis/dissertation in partial fulfillment of the requirements for a Postgraduate degree from the University of Saskatchewan, I agree that the Libraries of this University may make it freely available for inspection. I further agree that permission for copying of this thesis/dissertation in any manner, in whole or in part, for scholarly purposes may be granted by the professor or professors who supervised my thesis/dissertation work or, in their absence, by the Head of the Department or the Dean of the College in which my thesis work was done. It is understood that any copying or publication or use of this thesis/dissertation or parts thereof for financial gain shall not be allowed without my written permission. It is also understood that due recognition shall be given to me and to the University of Saskatchewan in any scholarly use which may be made of any material in my thesis/dissertation.

DISCLAIMER

Reference in this thesis/dissertation to any specific commercial products, process, or service by trade name, trademark, manufacturer, or otherwise, does not constitute or imply its endorsement, recommendation, or favoring by the University of Saskatchewan. The views and opinions of the author expressed herein do not state or reflect those of the University of Saskatchewan, and shall not be used for advertising or product endorsement purposes.

Requests for permission to copy or to make other uses of materials in this thesis/dissertation in whole or part should be addressed to:

Head of the Division of Biomedical Engineering
University of Saskatchewan
2B60 Engineering Building, 57 Campus Drive
Saskatoon, Saskatchewan S7N 5A9, Canada

OR

Dean
College of Graduate and Postdoctoral Studies
University of Saskatchewan
116 Thorvaldson Building, 110 Science Place
Saskatoon, Saskatchewan S7N 5C9, Canada

ABSTRACT

The current standard high-resolution peripheral quantitative computed tomography (HR-pQCT) based finite element (FE) models of distal radius sections explains 66% of variance in experimental testing results on intact forearms under fall configuration testing. However, this FE model employs a somewhat simplistic modeling approach in that it does not account for variations in mechanical properties within the radius, employs a fixed region of interest, and has been validated using embalmed samples, which can change forearm mechanical properties. Further, the effect of failure criteria on the predictions acquired using this model and their precision error is not known.

The aim of this study was to evaluate two different HR-pQCT-FE modeling approaches of distal radius for predicting failure load of the intact forearm under fall configuration testing. The purpose of study #1 was to evaluate the effect of failure criteria on wrist strength predictions acquired from HR-pQCT-based FE models *ex vivo* and their precision error *in vivo*. The purpose of the study #2 was to investigate the effect of using an anatomically standardized region of interest on FE predictions of distal radius failure load.

We acquired *in vivo* and *ex vivo* images of the distal radius via HR-pQCT. We performed failure testing on fresh-frozen forearms using a material testing system (MTS Bionix) to determine experimental failure load of forearms under fall configuration. We converted radius images to FE models using manufacturer-provided FE software. For the standard model, we used a single elastic modulus. For the density-based model, we used imaged bone mineral density to define elastic moduli.

In study #1 we derived failure loads for different failure criteria. The density based (E-BMD) model explained 91% of variance in failure load when using an energy equivalent stress criteria with critical volume and critical stress limits set to 0.1% and 70 MPa, respectively. $CV\%_{RMS}$ was 3.8% for the E-BMD model with highest R^2.

In study #2, we found that the failure loads were not different between the fixed and anatomically standardized (4% regions) ($p > 0.05$), and the fixed region and 4% region explained 89% and 87% variance in experimental failure load under fall configuration, respectively.

These findings indicated that the selection of failure criteria can alter the predictions of distal radius strength. Further, our results indicated that both single tissue and density-based HR-pQCT-FE models of distal radius sections can explain high variance (> 0.87) in failure load of intact forearms under fall configuration testing. Finally, the fixed and 4% regions provide similar predictions of distal radius strength for postmenopausal women.

PREFACE

Chapters 4 and 5 of this thesis have been drafted as coauthored manuscripts. I have provided contribution of the co-authors in both manuscripts below.

Manuscript 1 (Chapter 4):

Hosseinitabatabaei, S., Kawalilak, C., McDonald, M., Kontulainen, S., Johnston, J.D. HR-pQCT based finite element modeling of distal radius failure load using single tissue and density-derived modulus: Relationship with fall configuration forearm failure *ex vivo* and precision *in vivo*. *Submitted to BMC Musculoskeletal Disorders.*

Author's contribution: SH performed image analyses, finite element analysis, statistical analyses, data interpretation, and drafted and edited the manuscript based on feedback from co-authors. CK contributed to research protocol, data acquisition, analysis and manuscript edits. MM contributed to the research protocol and mechanical testing. SK contributed to the study design, research protocol, co-supervision of trainees, data acquisition, analysis and interpretation, and manuscript revisions. JDJ conceived the study idea, contributed to study design and research protocol, co-supervision of trainees, data acquisition, analysis and interpretation, and manuscript revisions.

Presentations at local and national conferences pertaining to this study:

i. **Hosseinitabatabaei, S.,** Kawalilak, C., McDonald, M., Kontulainen, S., Johnston, J.D. Estimation of distal radius failure load using HR-pQCT based finite element modeling: Selected model accuracy and precision. The 20th Biennial Meeting of the Canadian Society for Biomechanics, Halifax, Nova Scotia, August 2018.

ii. **Hosseinitabatabaei, S.,** Kawalilak, C., McDonald, M., Kontulainen, S., Johnston, J.D. *Ex vivo* Validation and *in vivo* Repeatability of HR-pQCT FE-based Distal Radius Bone Strength. 18th Annual Alberta Biomedical Engineering Conference, Banff, Alberta, November 2017.

iii. **Hosseinitabatabaei, S.,** Kontulainen, S., Johnston, J.D. Validating HR-pQCT-based Finite Element Predictions of Distal Radius Bone Strength.

Life and Health Sciences Research Expo, University of Saskatchewan, Saskatoon, Saskatchewan, May 2017.

iv. **Hosseinitabatabaei, S.,** Kawalilak, C., McDonald, M., Kontulainen, S., Johnston, J.D. Validating HR-pQCT-based Finite Element Predictions of Distal Radius Bone Strength. 17th Annual Alberta Biomedical Engineering Conference, Banff, Alberta, October 2016.

Manuscript 2 (Chapter 5):

Hosseinitabatabaei, **S.,** Johnston, J.D., Kontulainen, S. HR-pQCT based finite element models of the distal radius from the standard and anatomically standardized region do not differ and explain similar variance in experimentally-derived failure load. *Manuscript in preparation.*

Author's contributions: SH contributed to the research question, research protocol image analysis and segmentation, finite element analysis, statistical analyses, data interpretation, writing and editing the manuscript. JDJ contributed to study design, research question and protocol, supervision of trainees, data acquisition, analysis and interpretation, and manuscript revisions. SK contributed to study design, research question and protocol, supervision of trainees, data acquisition, analysis and interpretation, and manuscript revisions.

Presentations at an international meeting pertaining to this study:

i. **Hosseinitabatabaei**, **S.,** Soltan, N., McDonald, M., Kawalilak, C., Johnston, G., Kontulainen, S., Johnston, J.D. HR-pQCT finite element analyses of the standard region and 4% region offer similar predictions of distal radius failure load. HR-pQCT User's Meeting, Denver, September 2017.

AKNOWLEDGEMENT

Many thanks to my family in Iran for their patience and support.

I would like to thank my supervisors, Dr. James D. Johnston, and Dr. Saija Kontulainen for the patient guidance, encouragement, and advice through this research. Without their support this thesis would not have been completed.

I acknowledge the Discovery Grant funding from Natural Sciences and Engineering Research Council (NSERC) for funding the study, including half of my financial support.

Thanks to my advisory committee members, Dr. Allan Dolovich and Dr. Geoffrey Johnston, for their guidance.

I am grateful to the University of Saskatchewan and the Division of Biomedical Engineering for supporting me financially during this journey.

DEDICATION

I dedicate this thesis to my parents and sister for their support and encouragement.

TABLE OF CONTENTS

LIST OF TABLES

LIST OF FIGURES

LIST OF TERMS, ABREVIATION, AND SYMBOLS

TERM	DEFINITION
Anterior	Located closer to the front part of the body
Apparent modulus	The ratio of apparent stress and apparent strain within the elastic range
Apparent strain	Change in length over the original length of the whole bone model
Apparent stress	Reaction force over the projected cross-sectional area of bone model
Axial	Oriented along the longitudinal axis of body
Cortical bone	The compact bone tissue which covers the outer shell of the skeleton
Distal	Situated away from the center of the body
Dorsal	Located near the back (posterior of hand) in transverse plane
E-BMD	Elasticity-density equation or relation
Ex vivo	An experiment taking place outside a living organism
Harvesian canal	Microscopic canals in the cortical bone that contain blood vessels and nerves
In vivo	An experiment taking place inside a living organism
Isotropic material	A material with identical mechanical properties in different directions
Isotropic voxel	Voxel with same dimension in all directions
Lateral	Situated closer to the side of the body in the frontal plane
Medial	Situated closer to the middle of the body in the frontal plane
Medullary cavity	Central cavity of bone shaft where bone marrow is stored
Poisson's ratio	Ratio of transverse to longitudinal strains
Posterior	Situated closer to the back of the body in the transverse plane
Stiffness	The extent to which an object resist deformation

Strain	Ratio of change in length to the original length
Stress	Force acting on an area divided by the area

ABBREVIATION	DEFINITION
2D	Two dimensional
3D	Three dimensional
aBMD	Areal bone mineral density
BMD	Bone mineral density
BMC	Bone mineral content
DXA	Dual-energy x-ray absorptiometry
HR-pQCT	High-resolution peripheral quantitative computed tomography
FE	Finite element
PA	Posterior-anterior
WHO	World Health Organization
VOI	Volume of interest
ROI	Region of interest
BMC	Bone mineral content
CT	Computed tomography
E-BMD	Elasticity-density
STM	Single tissue model
DTM	Dual tissue model
HA	Hydroxyapatite
SD	Standard deviation
CV%	Coefficient of variation (in percent)
$CV\%_{RMS}$	Root-means-squared coefficient of variation (in percent)
PMMA	Polymethylmethacrylate
CaMos	Canadian Multi centre Osteoporosis
IPL	Image Processing Language

pQCT	Peripheral quantitative computed tomography
MTS	Mechanical testing system

SYMBOLS	DEFINITION
kV	kilo-volts
mA	milli-ampere
μm	micro-meter
E	Elastic modulus
S	Stiffness
σ	Stress
ε	Strain
ε_{eff}	Effective strain
F	Force
A	Area
L	Length
ν	Poisson's ratio (ratio of transverse to longitudinal strains)
Sv	Sievert (unit of ionizing radiation dose)
U	Strain energy density
mg	milli-gram
ρ	Density
U_x	Displacement in X direction
U_y	Displacement in Y direction
U_z	Displacement in Z direction

Chapter 1 Introduction

1.1 Overview

Osteoporosis is defined as "a skeletal disorder characterized by compromised bone strength predisposing to an increased risk of fracture." [2, 3]. About 200 million people worldwide are affected by osteoporosis and related fractures [4], which can cause pain, morbidity, and loss of independence [5]. Fractures caused by osteoporosis are usually categorized as fragility fractures and occur by a fall from a standing height or less. A wrist (distal radius) fracture, typically experienced during a fall onto the outstretched hand, is one of the most common osteoporotic fractures among older populations, especially in postmenopausal women [6]. It occurs when the external forces applied to bone (e.g., during fall onto outstretched hand) exceed bone strength, or bone failure load [7].

Individuals with osteoporosis who have suffered a wrist fracture have a greater risk of future osteoporotic wrist, hip and spine fractures [6, 8]. The incidence of wrist fractures peaks around age 65, approximately 10-15 years before peak incidences of hip and spine fractures [6, 9, 10]. Thus, assessment of wrist strength can provide early indication of further osteoporotic fracture risk [11]. Importantly, advanced imaging techniques can provide information of wrist strength and facilitate investigation of factors that enhance or deteriorate bone strength. Moreover, this information can be translated to research and preventative strategies for hip and other osteoporotic fractures.

Imaging techniques are important tools for assessment of wrist strength and bone properties. Dual-energy x-ray absorptiometry (DXA) imaging provides the operational definition of osteoporosis. This DXA imaging provides areal bone mineral density (aBMD) measurements [12]. Low aBMD values are associated with increased risk of fracture at the population level, while the predictive ability of aBMD for an individual person is poor [13], as it is shown that about half of fractures occur in patients considered non-osteoporotic using DXA [14]. In spite of the accessibility of DXA and its wide usage, currently, it is accepted that DXA is not sufficient since bone strength assessment requires information about bone geometry, mechanical properties, its microarchitecture, and load distribution, in addition to areal bone mineral density (aBMD) [13].

New imaging techniques, specifically high-resolution peripheral quantitative computed tomography (HR-pQCT), enable imaging of three-dimensional (3D) bone micro-architecture as well as volumetric BMD, with isotropic voxel sizes of 82μm. The "peripheral" nature of HR-pQCT limits its usage to peripheral sites such as the distal radius and tibia. HR-pQCT,

combined with finite element (FE) analysis, enables non-invasive assessment of the mechanical properties of bones at the forearm (e.g., failure load, stiffness, apparent modulus, apparent strength) *in vivo* [15, 16]. In general, FE models of bone are created directly by converting voxels representing bone tissue to equally-sized hexahedral brick elements, while bone marrow is ignored (i.e., the model consists of two materials, specifically bone and air). The number of elements is in the order of millions. These models are generally linear and do not simulate post-failure behaviour. Boundary conditions typically simulate a uniaxial compression test of a section of the distal radius, where failure is defined when a percentage of elements exceed a specific material strength (e.g., stress or strain limit).

As the usage of HR-pQCT combined with FE is relatively new, there is opportunity to evaluate the effect of different modeling approaches upon FE-estimated distal radius failure load. For example, it is unclear what effect inclusion of material property variation within the distal radius will have upon failure load predictions. At present, there is no universal agreement upon the selection of failure criteria for HR-pQCT-FE models. There is also a desire by many in the field to acquire HR-pQCT images from an anatomically standardized region (the current region is a fixed distance from the distal surface of the distal radius) [17, 18]; however, it is unclear what effect this will have upon FE-predicted failure load.

Accordingly, the overall aim of my thesis was to evaluate different modeling approaches applied to HR-pQCT-based FE models of the distal radius sections to identify specific approaches which were accurate (in relation to experimental failure testing of forearms) and precise. These approaches included addition of material property variation, evaluation of different failure criteria, and different scanning regions.

1.2 Scope of the thesis

Chapter 2 discusses the current literature, composition of bone, anatomy of wrist, forearm, and distal radius, medical imaging techniques, mechanical testing, and finite element method. In Chapter 3, research questions are outlined, and objectives are defined. In Chapter 4, the effect of failure criteria on the predictions of forearm failure load using HR-pQCT FE models and their precision errors are investigated. Chapter 5 compares the predicted forearm failure load from HR-pQCT FE models of the anatomically standardized region with those of the clinical (fixed) region. Limitations of this research and potential future work are outlined in Chapter 6.

Chapter 2 Literature review

2.1 Bone composition

Bone is one of the body organs which constitute the skeleton. Bone provides support for the body, protects vital organs, is a reservoir of calcium and phosphorus, contains blood-producing cells, and facilitates body movement [19].

The organization of bone is characterized as a highly hierarchical structure as shown in Figure 0-1. At the macro scale level, human bone tissue is generally classified as cortical and trabecular (cancellous). Cortical bone is found primarily in the shaft of long bones and the outer shell around trabecular bone at the proximal and distal ends of bones and the vertebrae, whereas trabecular bone is located within cortical tissue, in medullary cavities at the ends of long bones, and in the interior of short bones, such as spinal vertebrae. At the microscopic level, Haversian canals, osteons, and trabeculae can be observed. At the sub-microscopic level, lamellae are the basic building blocks of osteons and trabeculae. The nanostructure contains collagen fibrils which are made from the molecular structure of constituent elements, including organic and mineral phases, and water. The stiff and brittle mineral phase is an impure form of calcium phosphate, which is known as hydroxyapatite. The organic phase of bone mainly consists of type I collagen protein which provides toughness [20, 21].

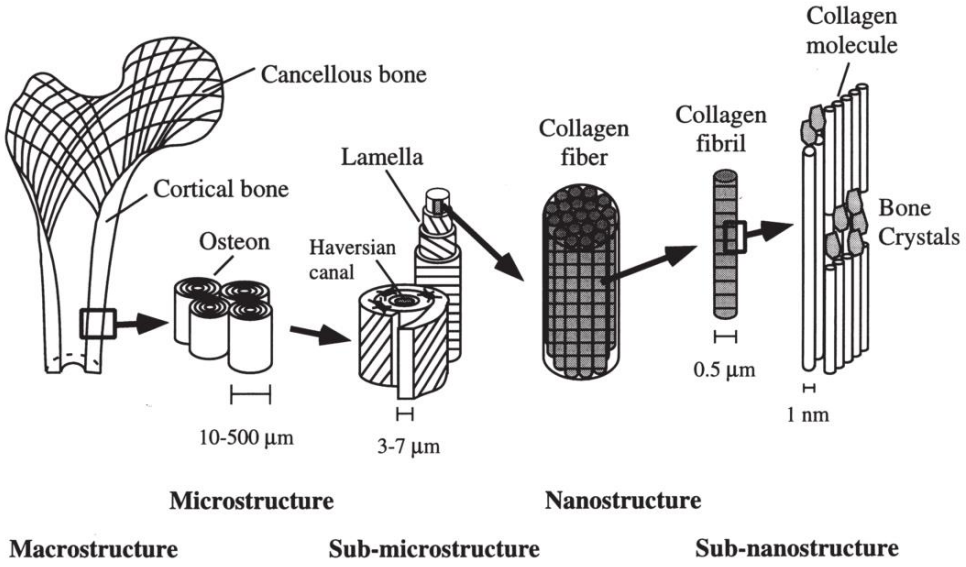

Figure 0-1. Hierarchical structural organization of bone at different scale levels (from left to right): cortical and cancellous (trabecular) bone; osteons and Haversian systems; lamellae; collagen fiber and fibrils; bone mineral and organic phases (Image from Rho et. al., [20]).

2.2 Anatomy

The wrist is one of the most complex joints in the body with a main role of facilitating movement of the hand. It is comprised of eight small bones, known as carpal bones, with the joints and ligaments enabling different motions. These bones connect the hand to the forearm. The bones are positioned in two rows, from which those on the proximal row are in contact with radius and ulna, which are forearm bones [22]. Carpal and distal forearm bones are depicted in Figure 0-2.

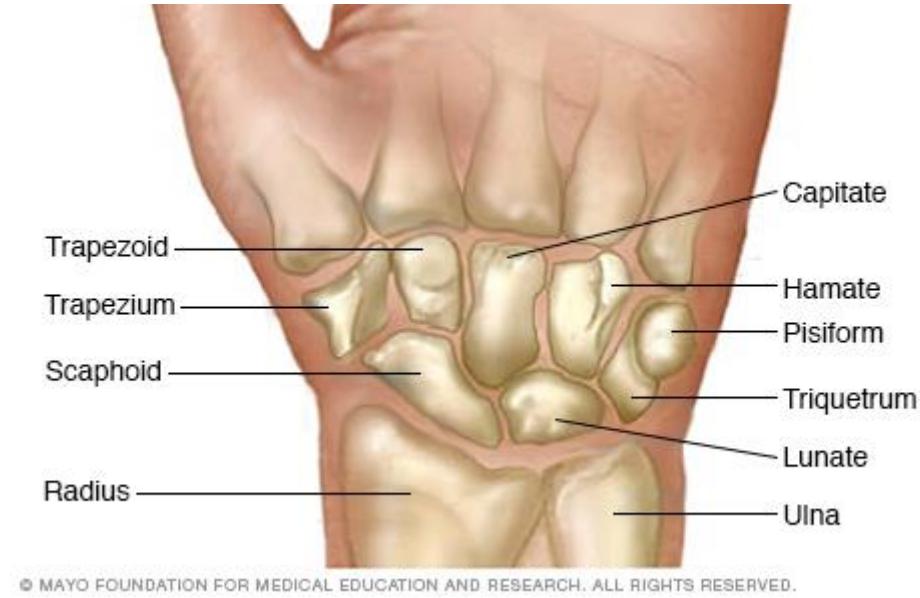

Figure 0-2. Illustration of carpal and distal forearm bones (adapted from MAYO foundation for medical education and research).

The radius and ulna are two large bones of the forearm [23]. As shown in Figure 0-3, in its distal part, the radial shaft expands to form a rectangular end. The lateral side projection of the radius is known as the styloid process, which serves as an attachment site for muscle and the lateral ligament complex. In the medial surface, there is a concavity known as the ulnar notch, which allows the radius to pivot around the head of the ulna. In addition, there are two other concave surfaces: the scaphoid and lunate facets, which articulate with the named carpal bones. Metaphyseal widening of the distal radius begins approximately 2 cm proximal to the radiocarpal joint [23]. Distal to this broadening, the amount of cortical bone decreases, and the corresponding amount of weaker cancellous bone increases, forming a zone predisposed to fracture (Figure 0-4) [24].

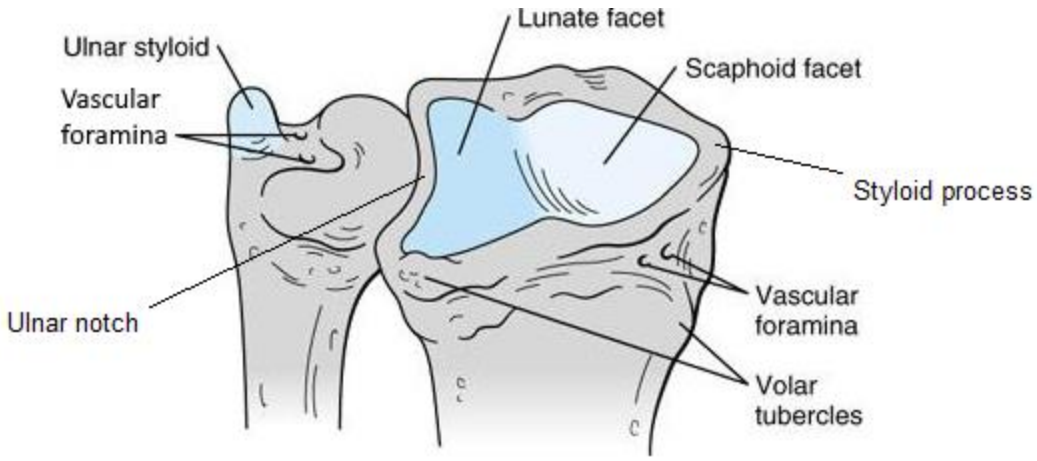

Figure 0-3. Anatomy of distal radius-ulna, indicating styloid process, ulnar notch, scaphoid, and lunate facets (adapted from Kaplan's Functional and Surgical Anatomy of the Hand, 3rd ed [23]).

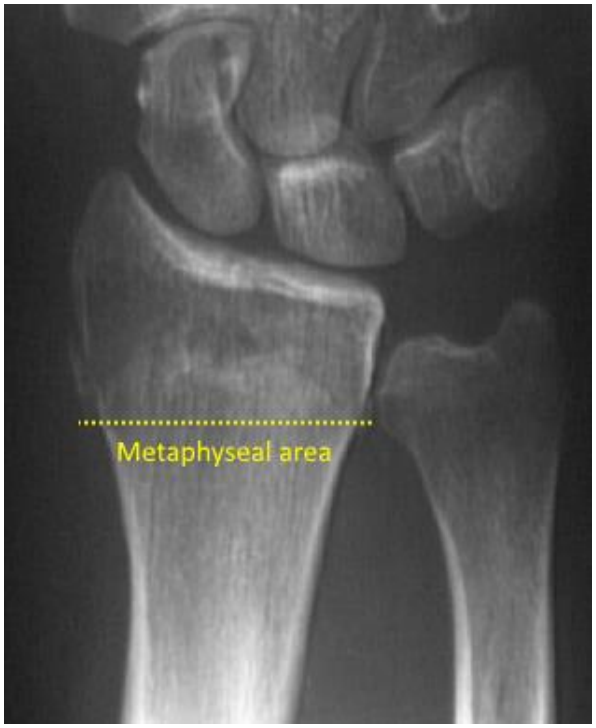

Figure 0-4 Frontal radiograph of distal forearm and wrist indicating the metaphyseal region.

The wrist usually undergoes several forms of loading, which are usually a combination of axial load, bending, and shear. In the case of a fall, only 15% of the cases exert an axial load to the forearm (i.e., axial component of the load is more dominant than bending and shear), which is usually due to a fall from backwards (falling directly onto the hand) [25]. However, in the majority of studies, only the axial loading is simulated [15, 26–29].

2.3 Types of fractures at distal radius

Distal radius fractures are frequently classified as: Colles', Smith, Barton, Hutchinson, and die-punch fractures [24].

Colles' fracture is a transverse fracture of the distal radial metaphyseal area with dorsal angulation and displacement of the distal fragment (Figure 0-5). It is the most common among distal radius fractures, and is generally produced by a fall on an outstretched hand [24].

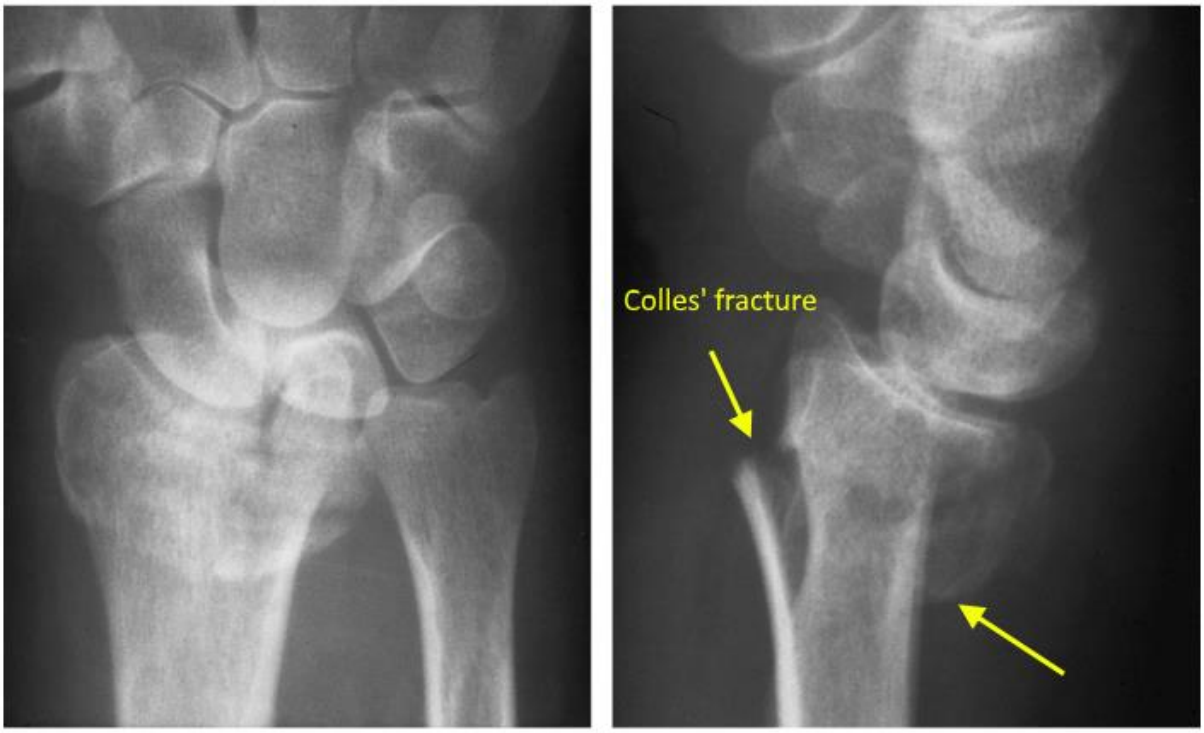

Figure 0-5. (a) Posterior-anterior radiograph of the left wrist demonstrating a distal radial fracture. (b) Lateral radiograph of the same wrist demonstrates a distal radius fracture with the distal fracture fragments displaced and angled dorsally relative to the proximal fracture fragment (Image from Goldfarb et.al., [24]).

A Smith fracture is a reversed Colles' fracture, in which the metaphyseal area undergoes a volar (palmar) angulation (Figure 0-6) [24]. A Barton fracture is a shear type fracture of the distal articular surface of the radius with lateral translation of the distal radius fragment with the carpus (Figure 0-7) [24].

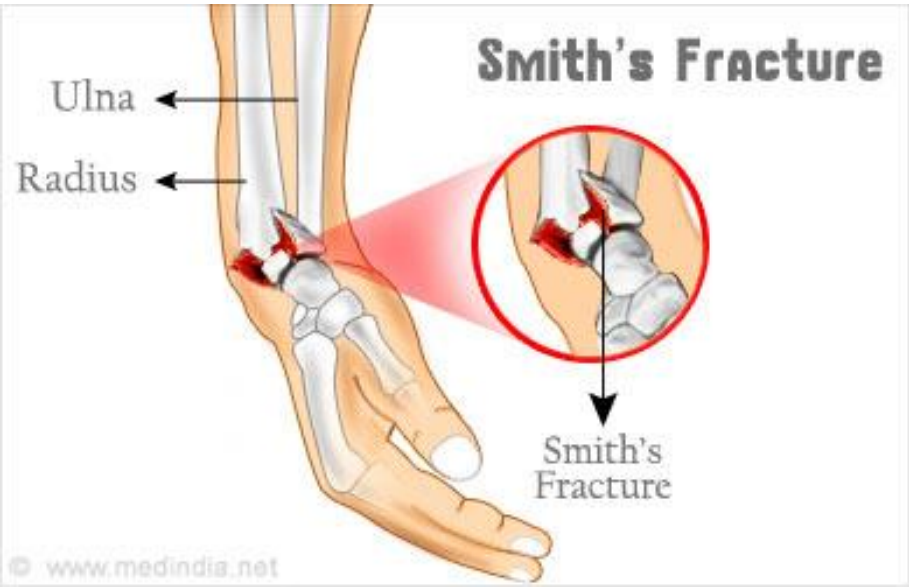

Figure 0-6. Schematic indication of Smith fracture with volar angulation.

Figure 0-7. (a) frontal and (b) lateral view of a dorsal Barton fracture (arrows) (Available online, case courtesy of Dr Aditya Shetty, Radiopaedia.org, rID: 28755).

A Hutchinson (chauffeur) fracture is defined as an oblique, intraarticular fracture of the distal radius, which involves the radial styloid (Figure 0-8) [24]. A die-punch fracture is a typical fracture of the lunate fossa of the distal radius (Figure 0-9) [24].

Figure 0-8. Frontal view radiograph showing a Hutchinson fracture at distal radius (arrows).

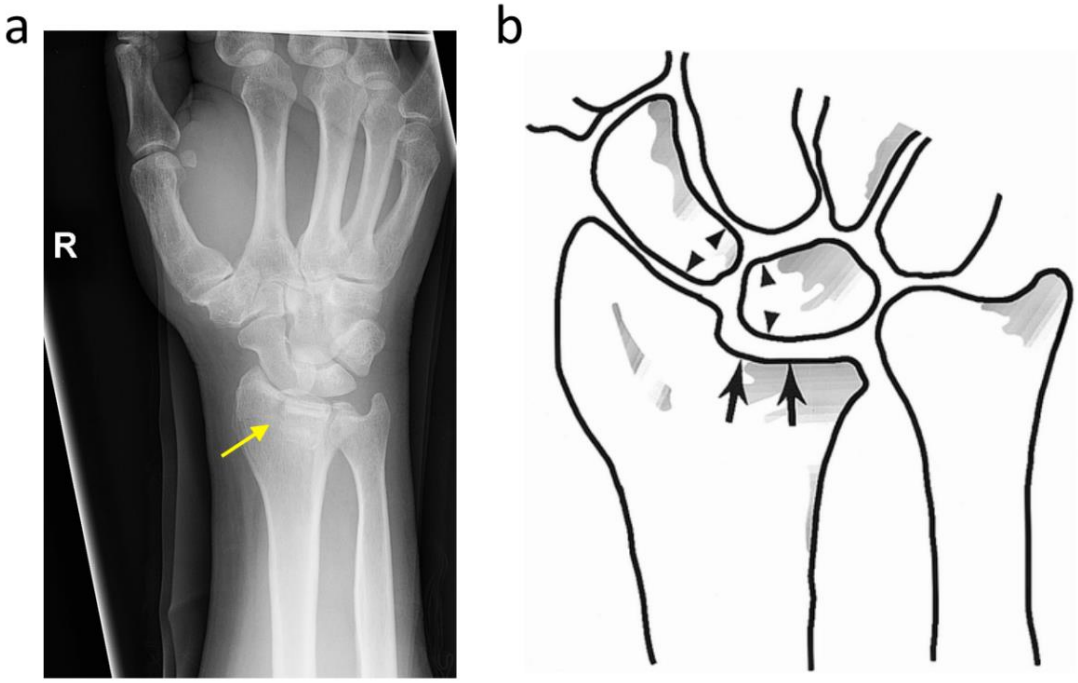

Figure 0-9. (a) frontal radiograph and (b) schematic view of die-punch fracture (arrows) (Available online, case courtesy of Dr Henry Knipe, Radiopaedia.org, rID: 38847).

2.4. Clinical estimation of bone fragility

2.4.1. Dual-energy x-ray absorptiometry (DXA)

Dual-energy x-ray absorptiometry (DXA) is the current standard method to estimate bone fragility through measures of areal bone mineral density (aBMD). As the name suggests, two x-ray beams with different energy levels are focused on the target site on body. One of the beams is mainly absorbed by soft tissue, while the other one by bone (i.e., attenuation). Then, BMD is determined from the attenuation levels of the soft tissue and bone. Since the DXA projection is a 2D image, BMD measured is usually referred to as areal BMD (aBMD).

Currently, aBMD values measured at the hip, spine, and forearm are used to determine bone density, including osteoporosis [30]. According to the World Health Organization (WHO), osteoporosis is defined as an aBMD that lies 2.5 standard deviations (or more) below the average aBMD for a young healthy person (T-score < -2.5) [31]. The T-score is calculated as follows:

$$T\text{-}score = \frac{Measured\ aBMD - Young\ adult\ mean\ aBMD}{Young\ adult\ population\ SD} \quad (2\text{-}1)$$

2.4.2 High Resolution peripheral Quantitative Computed Tomography (HR-pQCT)

Using HR-pQCT, bone micro-structure and BMD of the peripheral skeleton can be captured *in vivo*. As well, this imaging information can be integrated with FE modeling to derive mechanical properties of the distal radius. By simulating loadings on bone sections, mechanical properties such as failure load, stiffness, apparent modulus and strength can be estimated. Also, internal bone stress and strain can be predicted [32, 1]. With these outcomes, clinical research studies have investigated the effect of bone growth, diseases, medical treatments, and physical activity on bone mechanical properties, with a focus on bone failure load [33–36].

Currently, HR-pQCT images are acquired using the XtremeCT device (XtremeCT, Scanco Medical AG, Brüttisellen, Switzerland). To date, two generations of this device are manufactured. The first generation uses an X-ray tube with the scanning settings of 60 kV voltage, 1 mA current, 200 ms integration time, and 82 µm voxel size for *in vivo* imaging. According to the manufacturer recommended settings, a 9.02 mm area of distal radius is scanned using 110 parallel slices. It is located 9.5 mm proximal from the mid-region of the radial endplate (Figure 0-10). This selection is based on clinical studies and represents the metaphyseal area of distal radius. Within this region, major changes in cortical and trabecular

components occur such that the amount of cortical bone decreases, while the trabecular bone increases. Clinical studies have shown that the ultradistal radius (~3 cm) is where the majority of distal radius fractures occur which contains the 9.02 mm region. Eastell showed that Colles' fracture (the most common distal radius fracture) occurs 10 mm proximal to the landmark plateau (i.e., distal margin of the clinical region) [37]. The scanning time is about 3 minutes, and the radiation dose is less than 3 µSv per scan, which is low compared to the annual radiation dose for individuals (i.e., ~3 mSv in US). The second generation of XtremeCT HR-pQCT scanner (referred to as XtremeCT II) is capable of imaging bone with a voxel size of 61 µm and only a slightly higher radiation dose and shorter time. Our lab at the College of Kinesiology is equipped with the 1st Generation XtremeCT.

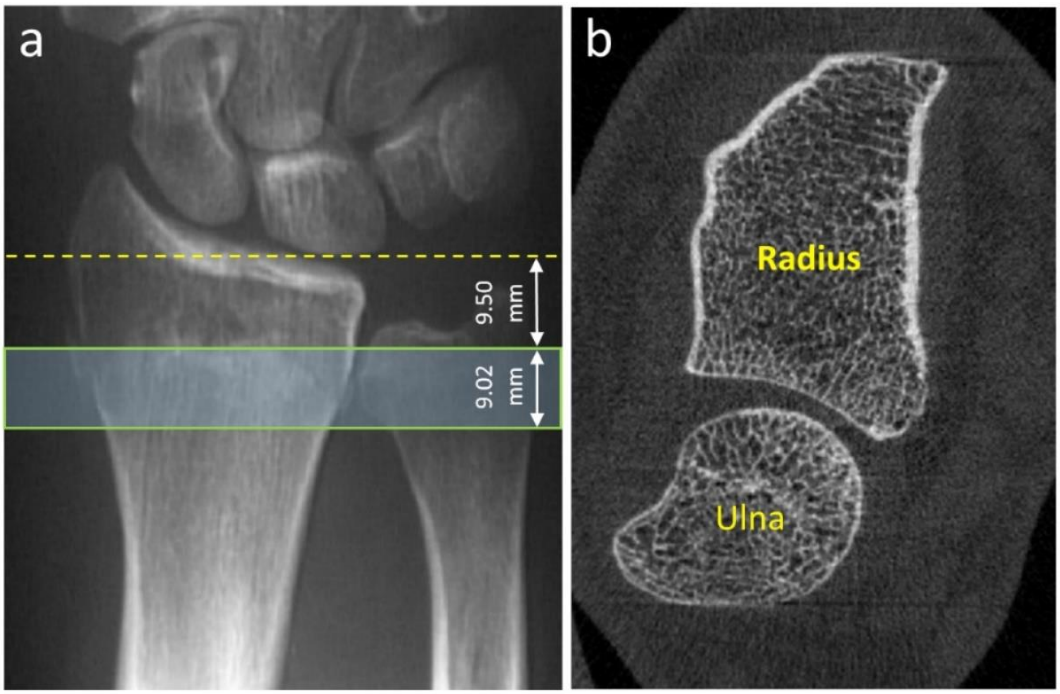

Figure 0-10. (a) Indication of the location of the standard (clinical) region of distal radius. The yellow line shows the reference line, and the green rectangle indicates the region b) Cross-section view of HR-pQCT scan of wrist (left forearm).

2.5. Mechanical testing

Mechanical testing is the gold standard to measure bone strength. Generally, for this area, the purpose of using a mechanical test is to quantify bone strength [38], correlate image-derived metrics to bone strength [39], then develop predictive models of bone strength [12, 27].

Mechanical testing of the distal radius has consisted of segments (e.g., pucks) acquired from the distal radius [27, 40–42], sole testing of the excised radius [28], and testing of the

intact hand-forearm [12, 26, 29]. With segment testing, individual segments are exposed to pure compressive loading to failure. With this approach, highly correlated values for apparent elastic properties (apparent modulus, stiffness) are reported ($R^2 > 0.97$). The high correlations are likely because the excised segments exactly match the region used in the FE analysis. However, this test though does not reproduce a forearm fracture during a fall and is more an indication of local strength of bone section versus forearm strength during a fall onto the extended hand. A few testing protocols have used the excised radius. However, they also have not been successful in consistently reproducing forearm fractures [43]. Of note, the studies which have used intact forearms have replicated forearm fracture patterns caused by a fall [12, 26, 29, 43]. Furthermore, intact specimens are more representative of the actual case of fracture and associated loading since they incorporate the effect of other tissues such as ligaments, joints, and the surrounding bones.

Furthermore, the type of the cadaveric specimens can affect the outcomes of the mechanical test. Two studies have shown that the fixation (i.e., embalming) of the cadaveric specimen can alter bone's mechanical properties including ultimate strength, maximum strain, modulus of elasticity, and hardness (i.e., likely due to prolonged exposure to formalin) [44, 45]. This suggests that using fresh-frozen specimens might be beneficial as their properties can be more similar to clinical conditions.

Experimental mechanical testing involves application of load or displacement against the object. From the progression of load or displacement in time, a load-displacement curve can be produced (Figure 0-11). The slope of the linear part of force-displacement curve is typically used to define stiffness. The failure load is the maximal load recorded before the bone breaks. The area under the curve is defined as the energy to failure. From the mentioned variables, failure load is the most widely used and reported as bone strength [1].

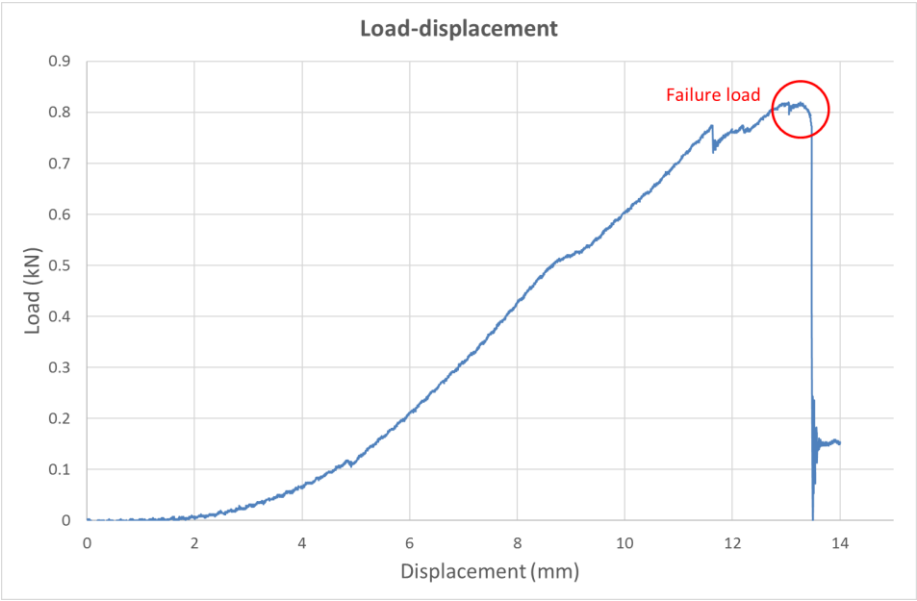

Figure 0-11. Typical force-time curve. Bone failure load is the maximal load recorded before the bone breaks, which could be observed on the load-displacement curve as the load after which a large drop occurred.

Table 0-1 summarizes studies which have performed uniaxial compression on distal radius bone segments, excised radius, or intact hand-forearm. They also performed HR-pQCT based FE analysis on bone sections. One of the main objectives of the following studies was to investigate how much variance in experimental failure load of forearms do the FE-derived failure loads from bone sections explain. The coefficient of determination for regression analysis is also provided in the table.

Table 0-1 Previous estimations of the relationships between HR-pQCT finite element (FE) estimation of distal radius failure load and experimentally derived distal radius or forearm failure load. R^2 indicates the explained variance in experimentally measured failure load by the FE derived failure load.

Study (ref. #)	**Specimens (n)**	**Specimen type**	**Sex**	**Mean age (SD)**	**Mechanical testing setup**	**FE model ROI**	**FE model type**	**FE material properties**	**FE critical value***	**FE critical volume (%)****	**R^2**	***In vivo* precision errors**
[12]	Intact forearm cadaver (54)	Embalmed	M & F	82 (9)	Axial compression onto outstretched hand	Distal 4 cm of forearm (carpal bones included)	Linear	Single material	7000 µstrain	1%-7%	0.75	Not studied
[26]	Intact forearm cadaver (54)	Embalmed	M & F	82 (9)	Axial compression onto outstretched hand	1cm region 6mm proximal to medial tip of radius endplate	Linear	Single material	7000 µstrain	2%	0.66	Not studied
[27]	9.1 mm bone sections (31)	Fresh-frozen	M & F	range: 55-93	Axial compression on bone sections	Same as samples	Linear & non-linear	Single & density-based material	NA	NA	>0.95***	Not studied
[28]	Intact radius bone (21)	Embalmed	M & F	82.2 (9.3)	Axial compression of excised radius	Clinical region + 9.02 mm adjacent to the most proximal point of subchondral endplate	Linear	Single material	7000 µstrain	2%	0.96	Not studied

[29]	Intact forearm cadaver (100)	Embalmed	M & F	80 (8.8)	Axial compression onto outstretched hand	5 consecutive VOIs with length of 4% of radius + the clinical region + all 5 regions	Linear	Single material	7000 μstrain	0.1%-95%***	0.78	Not studied
[40]	20.5 mm bone section proximal to the distal subchondral endplate (26)	Fresh-frozen	M & F	81.2 (13.7)	Axial compression on bone sections	Same as samples	Linear	Single material	7000 μstrain	2%	0.95	Not studied
[41]	9 mm bone sections (26)	Fresh-frozen	M & F	72 (11)	Axial compression on bone sections	Same as samples	Linear & non-linear	Single material	7000 μstrain	2%	0.92	Not studied
[42]	20 mm bone section 5 mm proximal to the lowest part of subchondral endplate (24)	Fresh-frozen	M & F	77.5 (9)	Axial compression on bone sections	Same as samples	Linear	Single material	7000 μstrain	2%	0.95	Not studied

* *Critical value: Stress or strain threshold for element failure*

** *Critical volume: Required percentage of failed elements, to fail the whole model*

*** R^2 *is reported for apparent stiffness*

2.6. Relationship between image properties and mechanical properties

For several years, different studies have investigated the accuracy of distal radius strength predictions from bone densitometric and structural parameters [46–48]. At early stages, only bone densitometric parameters including aBMD and bone mineral content (BMC) acquired from DXA images were available to estimate bone strength at the distal forearm. This measure does not provide information about the geometry of the bones or the distribution of the mineral content. Using DXA to predict radial fracture in a fall scenario using BMC, measured at the ultra-distal forearm site, was found to have a coefficient of determination of 0.53 [49]. Coefficient of determination for predicting forearm failure in a fall scenario using DXA scanning aBMD at the ultra-distal site of the radius was 0.60 [50].

In addition to bone mineral, bone geometry and micro-structure can be used to predict wrist strength using HR-pQCT. Also, HR-pQCT provides volumetric measurements of BMC and BMD. It has been shown that moderate predictions of fall configuration forearm failure load can be obtained by calculating these parameters on bone sections ($0.2 < R^2 < 0.7$). However, it is shown HR-pQCT-based predictions of fall configuration forearm failure load can be improved by using finite element analysis on the same bone sections since it incorporates bone geometry, micro-architecture, and mechanical properties [12]. Nevertheless, the effect of failure criteria on the fresh-frozen intact wrist strength predictions using such models in not known, in spite of its importance due to the linear nature of these models [29].

2.7. Finite Element Method (FEM)

FE analysis is a numerical technique used by engineers, scientists, and mathematicians to obtain solutions to (differential) equations that describe, or approximately describe, a wide variety of physical problems. It is based on dividing an object into a number of small finite elements of a simple geometry for which deformation and stresses can be calculated easily [1]. The FE method has been used to study biomedical tissues such as bone [1, 51–53].

Subject-specific FE analyses typically use CT datasets to define bone geometry and material properties [12, 15, 27, 1]. The FE method is preferable to the conventional method of using BMD or imaged strength estimates (e.g., area moment of inertia) to estimate bone strength since it incorporates variations in architecture as well as variations in bone mechanical properties, such as elastic moduli [15, 1, 54].

2.7.1. Discrete vs continuum FE

Subject-specific FE models are generally divided into two categories: (1) discrete models and (2) continuum models. With discrete models, bone microstructure is directly imaged and modeled. This is the standard approach used with HR-pQCT, where bone is typically assigned an elastic modulus of 10 GPa (though, others have employed 6.829 and 20 GPa) [12, 27, 29]. Continuum models are typically employed when bone microstructure cannot be directly imaged. This is the standard approach used when employing clinical CT image data. Because the micro-structure of the bone cannot be detected, elastic moduli are estimated from local BMD using published density-modulus equations derived from experimental data (e.g., $E = 15*(BMD/1200)^{1.7}$), commonly referred to as E-BMD models). Although discrete FE models are considered superior to continuum FE models (as they directly take into account the bone micro-structure), the method does not capture small variations in material properties (e.g., due to bone remodeling/modeling in response to exercise, drug treatment, etc). Accordingly, there is opportunity to account for material property variation when using HR-pQCT. To this end, there is no consensus on appropriate modeling parameters (e.g., density-modulus equation, failure criteria, measurement site) [27].

To date, two discrete FE models have been employed with HR-pQCT along with one continuum-based FE model. The discrete models include 1) homogenous single-tissue model (referred to as STM) which assigns the same material for all bone components (Figure 0-12 (a)) [12, 26]; and 2) homogenous dual-tissue model (referred to as DTM) which assigns different materials for trabecular and cortical bone [55]. The continuum-based "scaled" model defines heterogenous material properties via the E-BMD equation $E=15*(BMD/1200)^{1.7}$

(Figure 0-12 (b)) [27]. Based on *in vivo* studies, DTM is shown as a non-efficient method since it has not shown improvement in bone strength prediction, while requiring more human effort for manual segmentation [56]. STM does not account for variations in mechanical properties within bone; however, it predicted about 66% of variance in the fall configuration forearm failure load of embalmed specimens [12]. The "scaled" E-BMD model is a promising method as it accounts for small variations in mechanical properties and can be used to monitor changes in bone due to growth, diseases, and treatments. To date, the method has been used to validate FE-predictions of ultimate failure strength of segments of the distal radius. It is unclear whether the method accurately predicts distal radius failure load under a fall configuration testing setup.

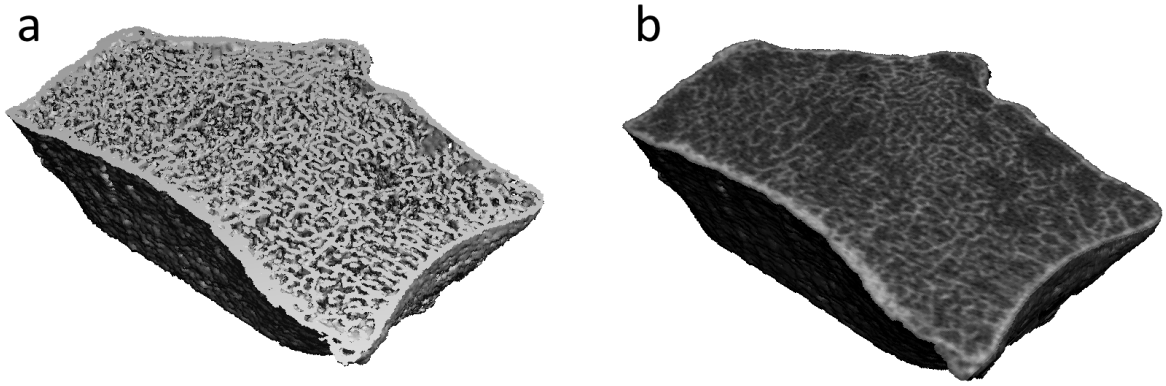

Figure 0-12 (a) Discrete (STM) and (b) continuum FE (E-BMD) models of the same distal radius bone section developed using HR-pQCT images.

2.7.2. Failure Criteria

Another consideration when performing FE analyses on bone is application of linear or non-linear modeling approaches. The advantage of a non-linear approach is that bone strength properties can be predicted directly [57, 58] and it is better suited for estimations of post-yield behavior [27]. However, non-linear models are computationally demanding, particularly for HR-pQCT-based FE models, which have millions of degrees of freedom [1]. Moreover, the results of a study by MacNeil and Boyd showed only modest improvements in bone strength prediction (specifically ultimate failure strength (stress)) using the non-linear approach when testing bone sections under axial compression (Table 0-1) [27]. With linear models, bone strength (failure load) is predicted using empirical relationships between FE-derived bone stress or strain and some strength metric (e.g., bone yield stress or strain). An example of a non-linear material model for bone is indicated in Figure 0-13.

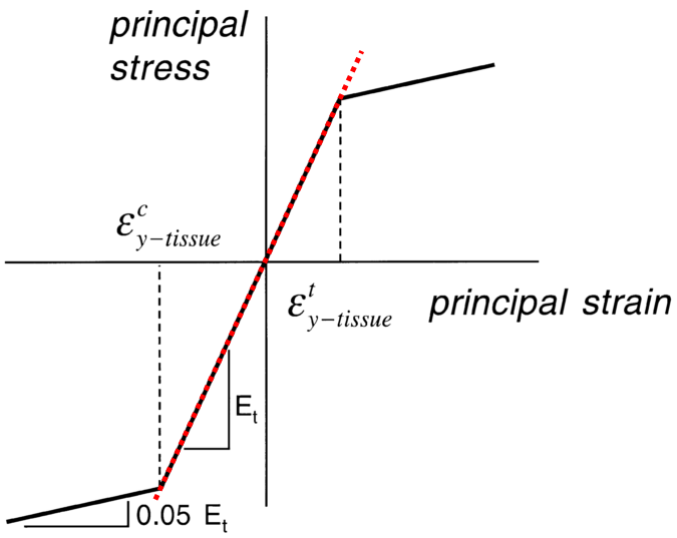

Figure 0-13 Bilinear constitutive model for bone (specifically for trabecular), which assumes that the elastic constants of the tissue were decreased isotropically when the principal strains exceeded either the tensile (ε^{c}_{y}) or compressive (ε^{t}_{y}) tissue yield strains [57]. Also, an example of a linear model is shown as red dotted line.

Accordingly, definition of the proper failure criteria is of utmost importance with linear models. Failure criteria can be categorized into stress-based and strain-based failure criteria, which are defined in terms of different mechanical parameters such as principal stress or strain, von Mises stress or strain, and energy equivalent stress or strain. From the mentioned parameters, energy equivalent strain has been widely used in past studies. This parameter is introduced by Pistoia based on non-linear FE studies by other researchers and is called *effective strain* [12, 57]. According to Pistoia's criteria, bone fails when 2% of the elements pass the tissue effective strain of 7000 μstrain. The effective strain is calculated from strain energy density and Young's modulus, as follows:

$$\varepsilon_{eff} = \sqrt{\frac{2U}{E}} \qquad (2\text{-}2)$$

where ε_{eff} is the effective strain, U is the strain energy density, and E is the Young's modulus. This failure criteria though is based upon discrete FE models with single material properties for bone. It is unclear if this criteria is appropriate when accounting for variations in material properties (i.e., elastic modulus (E) depends on BMD where maximum E of 15004 MPa corresponds to maximum BMD of 1200 mgHA/cm^3 of full mineralized cortical bone), where local strain is anticipated to be higher (due to the presence of bone with low elastic moduli). Moreover, the effect of failure criteria on the fall configuration forearm failure load predictions

using HR-pQCT FE models in not known, in spite of its importance due to the linear nature of these models [12]. To our knowledge, only Mueller et al. [29] have investigated the effect of different percentage of failed tissue on the accuracy of fall configuration forearm failure load [29]. However, they used embalmed samples, which can alter mechanical properties of bone (Table 0-1) [44]. Also, they have not studied the effect of failure criteria on precision errors of HR-pQCT FE derived failure loads.

Moreover, failure criteria can affect the precision errors of the FE models. Precision errors can characterize the reproducibility of a diagnostic technique [59]. In order to calculate the precision of repeated measurements on a patient root-mean-squared coefficient of variation, ($CV\%_{RMS}$) can be used, which is calculated as follows [59]:

$$CV\%_{RMS} = \sqrt{\sum_{j=1}^{m} \frac{\left(\frac{SD_j}{x_j}\right)^2}{m}} \qquad (2\text{-}3)$$

where SD_j is the sample standard deviation between the repeated measurements, x_j is the mean of the two measurements, and m is the number of participants in the analysis.

Precision of μFE is important to evaluate the repeatability of HR-pQCT-based strength measurements and to monitor changes in bone mechanical properties as a result of bone growth for children or bone degeneration in old patients, or to evaluate the effect of treatments. Although several studies have focused on the validity of the μFE models, only a few studies have investigated the precision of these models [56, 60, 61]. However, these studies have not calculated the precision errors for both STM and E-BMD models, and for different failure criteria. In one of these studies conducted by our group, Kawalilak et al. [56], estimated precision error for different HR-pQCT based FE models including the single tissue model (i.e., assigns single material to bone), dual tissue model (i.e., assigns different material to cortical and trabecular bones), and density-based model, using Pistoia's criteria for all of the models. Precision errors were comparable for all three models (<8.7%). However, it is not clear whether the precision errors for different failure criteria are comparable to the current model.

2.7.3. Region of Interest

Since the introduction of the HR-pQCT, the manufacturer has recommended a specific standardized scanning procedure (i.e., density calibration) and site (9.5mm proximal to the radial endplate). Only a few studies have evaluated whether alternate regions of interest would be better suited for predicting distal radius bone strength. Mueller et al., and Varga et al.,

showed that the most distal radius region improved prediction of distal radius fracture load when compared to the clinical region, with coefficients of determination of 0.76 vs 0.73 and 0.96 vs 0.92, respectively. Also, they showed that the most distal radius region results in less over-prediction of the distal radius fracture load (differences of 19% [29] and 13% [28], respectively). These findings though have not led to a change in the protocol of the selection of region of interest for HR-pQCT based prediction of distal radius bone strength, as the improvements in predictions of distal radius fracture load were not significant, and they did not report precision errors for different regions of interest.

In recent years there has been a push to change the region of interest from a fixed position to an anatomically standardized region due to anatomic variability in radius length, which can cause bias to group-wise comparisons between populations with different body sizes [18]. Other peripheral imaging techniques, such as standard peripheral quantitative tomography (pQCT), commonly use scanning protocols defining the region of interest based on limb length, with 4% of forearm limb length as being the most common distal imaging region [62, 63]. For HR-pQCT, using this anatomically standardized protocol, the location is defined relative to the length of the limb, with a recommended position at the 4% site of the radius length, measured from the medial tip of the endplate landmark [18]. This position matches the position used with pQCT [62, 63].

Pediatric HR-pQCT studies adapted an anatomically standardized distal radius region. Burrows et al. [64] introduced an anatomically standardized distal radius region for growing children and adolescents (to prevent radiation to the growth plate), with scans acquired at the 7% site of ulnar length. Kawalilak et al. implemented the 7% site to calculate precision errors of bone structural indices at the distal radius for children [65]. In adult populations, Shanbhogue et al. [17] acquired images from the 4% region at the distal radius using HR-pQCT. In this work, they compared the morphologic and density measurements acquired from the standard and the 4% regions. A recent study by Bonaretti et al. [18] on adults compared HR-pQCT outcomes with fixed versus anatomically standardized (i.e., 4%) regions and reported large differences between the different HR-pQCT outcomes (2.4% - 19.5%). However, it is currently unclear what effect a new region of interest will have upon FE-predictions of distal radius bone strength.

2.8 Summary

- Distal radius fracture, which is a type of wrist fracture, is the most common osteoporotic fracture among older populations, especially postmenopausal women. It typically occurs when a person falls onto the outstretched hand, when external forces applied to bone exceed bone strength.
- High-resolution peripheral quantitative computed tomography (HR-pQCT) enables imaging of three-dimensional (3D) bone micro-architecture as well as 3D BMD. HR-pQCT, combined with finite element (FE) analysis, enables non-invasive assessment of the mechanical properties of the distal radius (e.g., failure load, stiffness, apparent modulus, apparent strength) *in vivo*.
- The current HR-pQCT based FE model has been used in many studies as a replacement for the conventional indices including densitometric (e.g., BMD) or structural parameters to predict fall configuration forearm failure load, and has moderately improved such predictions. However, the current standard model has a few limitations including assuming a single material for bone and using embalmed samples for validation (Table 0-1).
- We proposed the following approaches to improve intact wrist strength predictions derived from HR-pQCT based FE models: addition of material property variation, evaluation of different failure criteria, and different scanning regions. Also, no study has performed mechanical testing on fresh-frozen intact forearms (Table 0-1).
    - Material variation: the standard model assigns a single elastic modulus to bone. Assigning material properties based on bone density (density-based model) can improve estimation of intact wrist strength using HR-pQCT FE models. Although a density-based model is used, its strength indices are only related to those of the mechanical test on bone sections (Table 0-1).
    - Failure criteria: due to the linearity of the standard model, the failure criteria plays an important role. To date, a few studies have tried different failure criteria. However, those studies were limited to strain-based failure criteria, mainly Pistoia's criteria. Also, the precision of different failure criteria is not reported (Table 0-1).
    - Different scanning region: the standard model uses a bone section model at a fixed distance from the radiocarpal joint. However, anatomic variability in bone length can cause bias in population study comparisons. A few studies have shown that the volume of interest for the FE model affects the predictions of wrist strength. To

date, the effect of using an anatomically standardized region on FE-derived bone strength indices has not yet been studied.

Chapter 3 Research questions and objectives

Given the gaps in the literature, my specific research questions are:

a) Which FE modeling approach (STM or E-BMD model) and failure criteria (i.e., strain based or stress based criteria with different percentages of failed tissue) of distal radius models predicts the most variance in forearm failure load under fall configuration testing?
b) Which FE model (STM or E-BMD model) and failure criteria lead to the most precise prediction of forearm failure load under fall configuration testing?
c) Is there a difference between FE-derived failure loads acquired from the fixed and 4% regions of the distal radius?
d) How accurate are the predictions of intact forearm failure load from the fixed and 4% regions?

To address these questions, my objectives were as follows:

1. To apply two HR-pQCT FE modeling approaches (STM and E- BMD) and failure criteria (i.e., strain based or stress based criteria with different percentages of failed tissue) on distal radius images and identify methods predicting most of the variance in forearm failure load acquired using fall configuration experimental testing *(addressed in Chapter 4).*
2. To define *in vivo* precision errors for the different FE modeling approaches (STM or E-BMD) and failure criteria *(addressed in Chapter 4).*
3. To investigate if there is a significant difference between distal radius failure loads acquired from the fixed and 4% regions *(addressed in Chapter 5).*
4. To evaluate explained variance in the experimentally-derived forearm failure load of fall configuration test acquired with HR-pQCT FE analyses of the fixed and the 4% regions *(addressed in Chapter 5).*

Chapter 4 HR-pQCT based finite element modeling of distal radius failure load using single tissue and density-derived modulus: Relationship with fall configuration forearm failure load *ex vivo* and precision *in vivo*

4.1. Introduction

The current FE model used with HR-pQCT simulates pure compression testing of bone cross-sections of the distal radius, akin to experimentally testing large bone biopsies in a material testing system. This model offers a failure load associated with the pure compression test. This model has several advantages including a relatively short scanning time (~3 minutes), low radiation dose (~3 μSv) and simple loading conditions. However, compression testing on distal radius bone sections does not necessarily simulate the loading conditions or fracture type associated with a fall [43]. More importantly, the failure load associated with the standard pure compression test may not reflect the failure load associated with a fall.

Employing fall configuration testing on intact forearm or radius offers representative loading conditions, fracture types (i.e., Colles), and failure loads [43]. Unfortunately, FE modeling of the intact forearm or radius is not feasible for clinical use due to limited computational resources and complexity of modeling and loading conditions. On the other hand, HR-pQCT FE models of distal radius bone sections (with correct material property assignment and failure criteria) may be sufficient to estimate forearm failure load during a fall.

Research to date indicates that FE models of sections of the distal radius explain approximately 66-73% of the variance in experimentally-measured forearm failure load under fall configuration testing [12, 29]. Prior studies [12, 26, 29] were limited to the use of embalmed samples, with embalming being known to alter the mechanical properties of bone [44, 66]. Prior validation studies also applied the failure criteria established by Pistoia et al [12], where failure was assumed to occur when 2% of bone tissue exceeded an energy-equivalent strain limit of 7000 μstrain. It is unknown if alternate failure criteria (i.e., stress criteria and different percentages of strained tissue) may improve predictions of forearm failure load measured from fall configuration testing. Prior research also modeled the distal radius as being comprised of either bone or air (i.e., single tissue model or STM), where bone was defined via a threshold [12, 26, 28, 29]. MacNeil and Boyd [27] developed a density-based FE model (referred to as E-BMD) which derives elastic moduli (E) throughout the distal radius in relation to imaged BMD. A benefit of this E-BMD model is its potential to capture differences in bone tissue mineralization which may be missed by the STM method. This is important because bone growth, aging, diseases, or treatments may change bone tissue mineralization, which can affect

strength by changing the stiffness, toughness, and ductility of bone [27, 67, 68]. Another advantage of the E-BMD model is that it may help to compensate for partial volume effects since it does not require segmentation of bone microstructure [69]. MacNeil and Boyd [27] previously validated the use of the E-BMD model for predicting apparent strength (ultimate stress) of distal radius sections, but failure load remains to be validated using this model.

In addition to accurate predictions of forearm failure load, it is vital to identify the error between repeated measurements (i.e., precision error or repeatability). This is important because a specific failure criteria may offer strong predictions of failure load yet have a poor precision error (especially *in vivo)* indicating high variability within the data. To date, a few studies have investigated the precision error of FE-derived failure load for cadavers [61], young adults [60] and postmenopausal women [56]. All these studies though have estimated failure load using Pistoia's failure criteria [12, 56]. There are not yet precision metrics for different failure criteria (i.e., stress-based or strain-based criteria with different failed tissue percentages).

Accordingly, our first objective was to apply two HR-pQCT FE modeling approaches (STM and E-BMD) and different failure criteria (i.e., strain-based or stress-based criteria with different percentages of failed tissue) on distal radius images to identify the method which best explained variance in intact forearm failure load acquired using fall configuration experimental testing. Our second objective was to define *in vivo* precision errors for the different FE modeling approaches (STM or E-BMD) and failure criteria.

4.2. Methods

4.2.1. Specimens and participants

For the experimental study, we acquired a sample group of nineteen (n=19) fresh-frozen cadaveric forearms of older females from an anatomical tissue bank (mean age (standard deviation, SD): 83.7 (8.3) years). We selected specimens from older female donors without a history of fracture or bone disease and with BMI < 25. These donors were representative of the population at higher risk of forearm fracture [70, 71]. We cut away soft tissue from around the radius and ulna (wrist joint and hand left intact), and potted the midshafts in polymethylmethacrylate bone cement (PMMA) according to the method explained by Edwards & Troy [72]. The specimens were kept frozen at -20°C and were thawed at room temperature prior to sample preparation, image acquisition, and mechanical testing.

For the precision study, we further assessed a random subsample of 28 postmenopausal women (74 (7) years) from the Saskatoon cohort of the Canadian Multi-centre Osteoporosis (CaMos) study [56]. Details of this cohort and subsample were provided previously [56]. We obtained participant consent prior to the study. All procedures were approved by the University of Saskatchewan Biomedical Research Ethics Board.

4.2.2. HR-pQCT imaging

We imaged the forearms using the first generation HR-pQCT (XtremeCT I; Scanco Medical AG, Brüttisellen, Switzerland) with an isotropic voxel size of 82 µm (60 kV, 1 mA current, 200 ms integration time, and 1536 × 1536 pixels image matrix). We used the standard protocol, as described elsewhere [28, 29, 56]. The standard 9.02 mm region of interest (110 parallel slices) was scanned. Each scan took about 3 minutes for each forearm. For the precision study, we scanned the forearms of the postmenopausal women using the standard protocol at two time points, ten days apart (mean (SD) 10 (4) days) [56].

We performed image segmentation based on the manufacturer's standard evaluation protocol (Scanco Module 64-bit IPL V5.08b). We used a semi-automatic edge-finding algorithm by applying a fixed global threshold (400 mgHA/cm^3) to segment the distal radius from the surrounding soft tissue, followed by manual correction. A single investigator (SH) manually corrected segmentation of cadaveric images and another investigator (CK) corrected postmenopausal images [56].

4.2.3. FE analysis

For both experimental and precision studies we used the manufacturer-provided FE software (Image Processing Language, IPL; version 1.15) for FE analyses. We created models by directly converting the isotropic voxels of the HR-pQCT images to same size 8-node brick elements of 82 µm. Each model was composed of ~2.5 million brick elements. Bone material properties were treated as exhibiting isotropic, linear elastic material behavior. For the standard STM approach, we assigned a tissue elastic modulus of 6.829 GPa to all bone elements [27]. For the density-based E-BMD approach, we assigned elastic moduli using the following density-elasticity equation [27, 56, 69]:

$$E = 15,004\left(\frac{\rho}{1200}\right)^{1.7} \quad (4\text{-}1)$$

where ρ is the density (mgHA/cm^3) of each voxel and E is the elastic modulus (MPa) [27]. Poisson's ratio was set to 0.3 for both STM and E-BMD approaches [27].

We simulated a “high friction” axial compression test by constraining the nodes of the most proximal surface in all directions and applying a 1% axial compressive strain to the distal surface of the bone section (Figure 0-1) [15]. We defined failure of the models based on empirical relationships from the literature [12, 57]. First, we used the failure criteria established by Pistoia et al., where failure was assumed to occur when 2% of bone tissue, referred to as the critical volume, exceeded an energy equivalent strain limit of 7000 μstrain [12, 57]. The corresponding load at the critical strain limit represented the failure load. We also defined failure loads corresponding to different critical volumes ranging from 0.06% to 7.5%. For the E-BMD model, we obtained a range of failure loads using energy equivalent strain and energy equivalent stress failure criteria (with the limits of 7000 μstrain and 70 MPa, respectively) with different critical volumes (0.06%-7.5%). Both stress and strain failure criteria were applied due to the heterogeneous nature of the E-BMD model, which could lead to incorrect failure load estimates due to the high presence of bone elements with low elastic moduli. Using the standard Scanco workstation, each model was solved in ~3 hours for STM and ~5 hours for E-BMD.

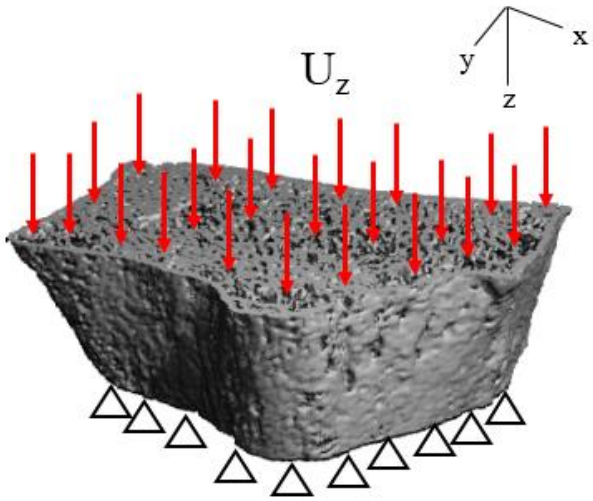

Figure 0-1 μFE model with boundary conditions, where U_z is the uniform compressive displacement acting on the distal (upper) surface of bone, while the nodes of the distal surface are fixed in x and y directions. Nodes of the most proximal (lower) surface are fixed in all directions.

4.2.4. Mechanical testing

After HR-pQCT imaging, we performed axial compression testing on the intact forearms using a material testing system (MTS Bionix Servohydraulic Testing System) to measure the experimental failure load (Figure 0-2). The goal of the test was to simulate fracture as a result of a fall onto the outstretched hand [43, 46]. Thus, we mounted forearms vertically with 0° dorsal inclination and 3-6° radial inclination, such that the palm was flat against the testing

plate [46]. Axial compression was applied at 3 mm/s onto the palm of the hand until fracture [12, 72]. Using the force-displacement curve, the ultimate failure load for each specimen was determined. Specifically, failure was assumed to occur when the force rapidly dropped after reaching a maximum peak.

From the 19 specimens mechanically tested, 5 specimens did not experience a distal radius fracture and were excluded from further analysis (the excluded specimens experienced: wrist dislocation (n = 2), and fractures of the scaphoid (n = 1), ulna (n = 1), and hand (n = 1)). We also excluded data from one specimen as it was an outlier with a standardized residual more than 2.5 units away from the zero value [73]. The final number of samples for our regression analysis was 13.

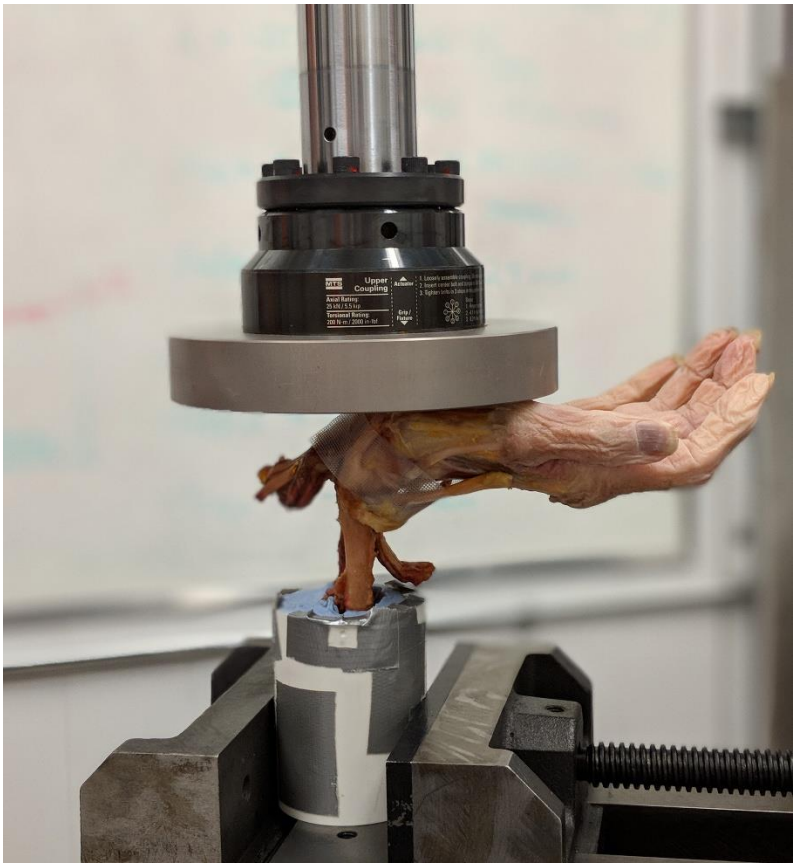

Figure 0-2 Testing setup for uniaxial compression on intact forearm. Compressive load was applied on the palm of the outstretched hand until fracture.

4.2.5. Statistical analysis

For our first objective, we assessed relationships between FE-derived and experimentally measured failure loads using linear regression. We report coefficients of determination (R^2) for each model and identified the distal radius FE model and failure criteria that best explained variance in forearm failure load. For our second objective, we report root-mean-squared

coefficient of variation ($CV\%_{RMS}$) to define short-term in vivo precision errors for different FE estimates of distal radius failure load from different models and failure criteria [56, 59]. We also report 90% confidence intervals for $CV\%_{RMS}$ calculated using the equation shown below [59].

$$\frac{df}{\chi^2_{\frac{\alpha}{2},df}}(CV\%_{RMS})^2 < \sigma^2 < \frac{df}{\chi^2_{1-\frac{\alpha}{2},df}}(CV\%_{RMS})^2 \quad (4\text{-}2)$$

where, df is the degrees of freedom, $CV\%_{RMS}$ is the short term precision error of the technique, and χ^2 is the chi-square distribution of the desired confidence (1-α) with the degrees of freedom of df. χ^2 values can be found from a variety of sources [74].

4.3. Results

4.3.1. Objective 1- Regression analysis

The standard model (STM) explained 87% to 89% of variance in the experimental forearm failure load (Figure 0-3 (a)). Pistoia's 2% critical volume criteria explained 89% of the variance in forearm failure load (Figure 0-4 (a)), which was also the highest explained variance (Figure 0-4 (b)).

The E-BMD model using the energy equivalent strain criteria explained between 86% to 90% of the variance in forearm failure load (Figure 0-3 (b)). Pistoia's 2% criteria explained 87% of the variance (Figure 0-4 (c)) while a critical volume of 0.06% explained 90% of variance in failure load (Figure 0-4 (d)).

The E-BMD model using energy equivalent stress criteria explained between 34% to 91% of the variance in forearm failure load (Figure 0-3 (c)). Pistoia's 2% criteria explained 73% of the variance (Figure 0-4 (e)) while a critical volume of 0.1% explained 91% of variance (Figure 0-4 (f)).

4.3.2. Objective 2 - Precision errors

Precision errors with the standard model ranged between 2.6 % and 3.7%, with an error of 2.9% corresponding with Pistoia's 2% criteria (Figure 0-3 (a)). Precision errors with the E-BMD model using an energy equivalent strain criteria were approximately 5% for all critical volumes ($CV\%_{RMS}$ ranged between 4.8% and 5.1%) (Figure 0-3 (b)). Precision errors with E-BMD model using an energy equivalent stress criteria ranged from 2.6% and 4.6% (Figure 0-3 (c)).

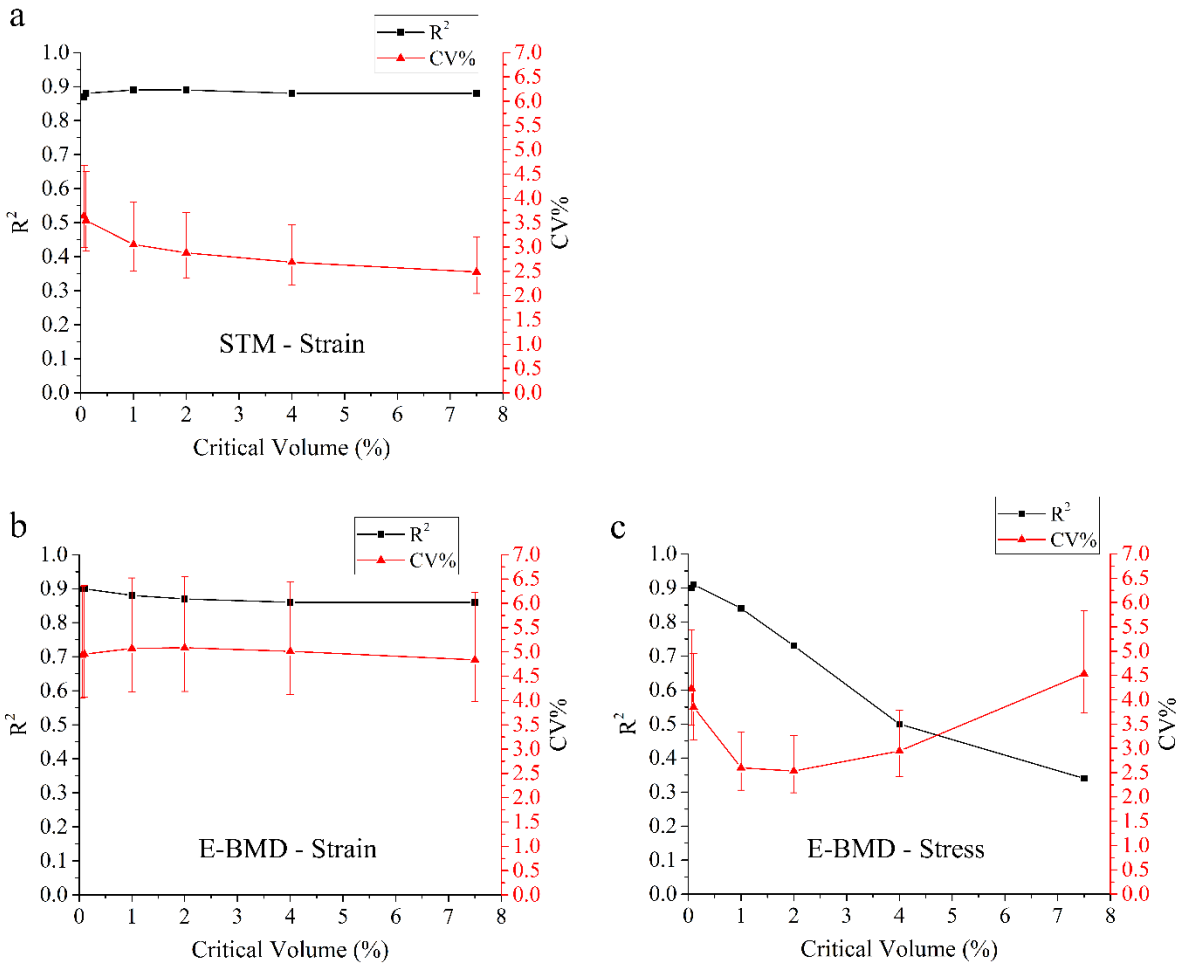

Figure 0-3 Changes of coefficient of determination (R^2; black) and precision error ($CV\%_{RMS}$; red) with critical volume for (a) STM, (b) E-BMD model with energy equivalent strain and (c) energy equivalent stress failure criteria. Error bars represent 90% confidence interval for precision errors.

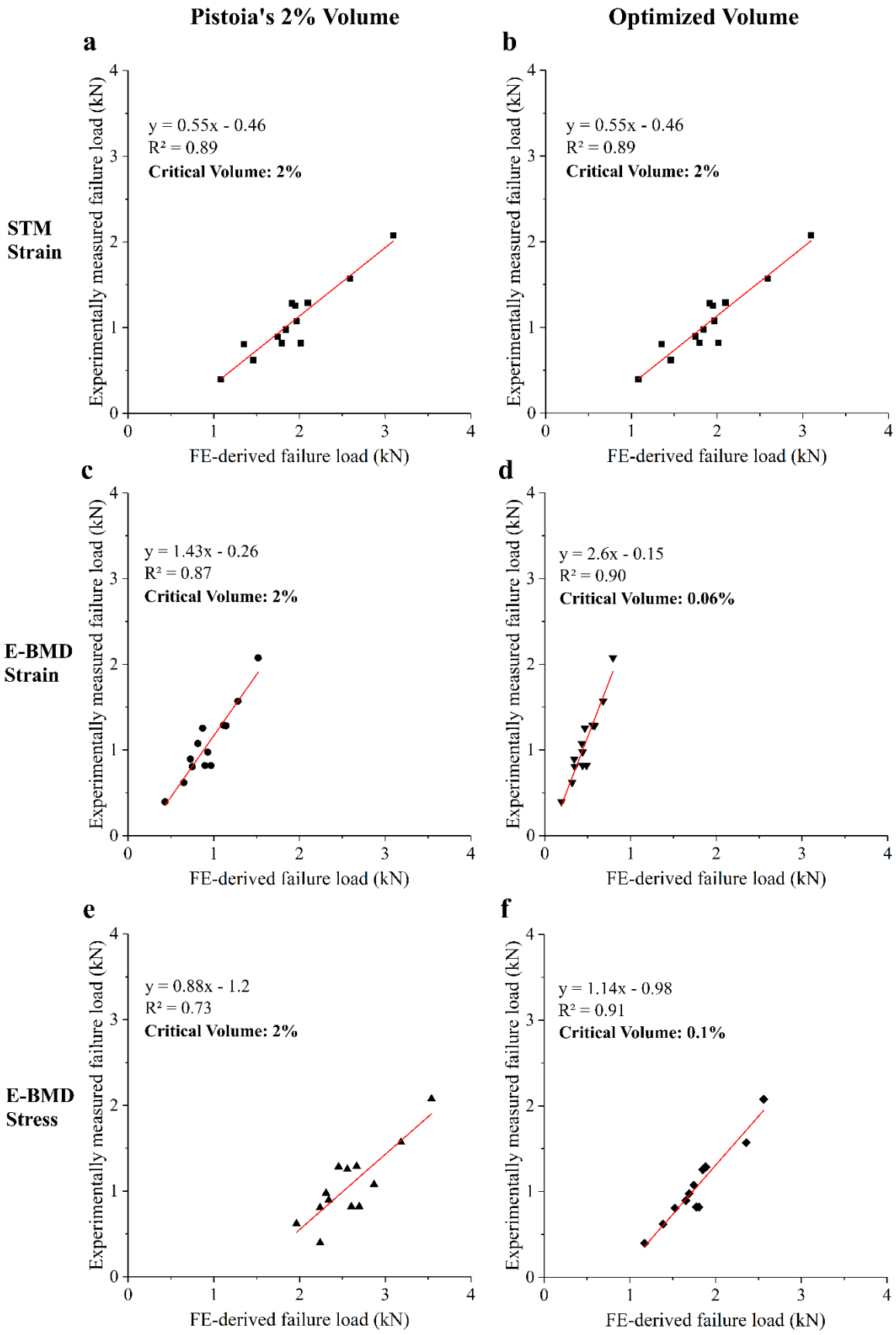

Figure 0-4 Linear regression results for Pistoia's 2% criteria for each model (left) with linear regression for models with best fit (highest R^2) (right) (a) STM model with energy equivalent strain

and critical volumes of 2% (Pistoia's 2% failure criteria), and (b) 2%, (c) E-BMD model with energy equivalent strain and critical volumes of 2%, and (d) 0.06%, (e) energy equivalent stress with critical volumes of 2% and (f) 0.1%.

4.4. Discussion

Our first objective was to apply different modeling approaches and failure criteria to HR-pQCT FE models of the distal radius sections to identify the method which best predicted fall-configuration forearm failure load. Our results indicated that STM and E-BMD approaches using strain-based failure criteria explained similar variance in forearm failure load ($R^2 \approx 0.88$) regardless of the selected critical volume. In other words, changing the failure criteria appeared not to affect explained variance in failure load when using the standard model (STM) or the strain-based E-BMD model. Conversely, when using stress-based failure criteria our results indicated that the E-BMD model appeared to be markedly affected by the critical volume. Specifically, with a smaller critical volume (0.1%), R^2 was 0.91 in comparison to 0.34 with high critical volume (7.5%). Therefore, the selection of failure criteria is important when performing HR-pQCT FE analyses of the distal radius.

To our knowledge, the current study has provided the highest explained variance in experimental failure load of intact forearms under fall configuration test using HR-pQCT based FE models of distal radius bone sections. However, a statistical comparison is not feasible between the results of this study and previous studies [26, 29], mainly because of the differences in the samples (e.g., embalmed cadavers compared to our use of fresh-frozen cadavers). By using fresh-frozen specimens we could avoid changes in bone mechanical properties caused by embalming. This study also gave insight into the effect of modeling approaches in terms of material properties (STM vs E-BMD) and failure criteria on predictions of fall configuration forearm failure load using HR-pQCT FE models of distal radius sections and their precision errors. The results of this study provided further evidence that HR-pQCT-based FE models of distal radius bone sections can be used as a clinical tool to predict forearm bone strength during a fall.

The results of our study both agree and contrast with those of Mueller et al. [29]. Similar to our results with the STM model, their range in R^2 with different critical volumes was limited. On the other hand, they found that Pistoia's 2% criteria explained 73% of variance in forearm failure load [29] while our model explained 89%. This discrepancy may be due to the use of embalmed forearm specimens, as embalming can affect the mechanical properties of bone [44,

66]. This may also be because of including samples from both males and females in their study. The location of fracture might be different for males and females due to the difference in limb length, and the fracture might not be inside the region of interest used for FE analysis. Also, the values of failure load might be different between males and females (i.e., likely the failure load for males is larger than females). As a result, including the failure loads from both males and females in a single regression analysis might have reduced the coefficient of determination of the regression.

Our results for the E-BMD model indicated the importance of failure criteria selection. When using strain-criteria, R^2 ranged between 0.86 to 0.90 for different critical volumes. Conversely, with the stress-criteria, R^2 ranged between 0.34 to 0.91. This difference likely originated from the heterogeneity of elastic moduli among elements. When using the strain-based failure criteria with the E-BMD model, the elements with lower elastic moduli (E) may contribute to bone failure while the elements with high elastic moduli likely contribute to the stress-based criteria. To clarify, since the E-BMD model scales BMD to define elastic moduli, the model inherently has a number of bone elements with low elastic moduli. These bone elements will reach the critical 7000 μstrain limit with low loads, which can yield failure load values which are not realistic. Conversely, the stress analysis is mainly focused on elements with high E rather than low E, which results in failure load values comparable to those of the standard model, as found in our prior research [56]. Accordingly, a stress-based criteria should alleviate this potential issue and be a better metric for failure load predictions using HR-pQCT-based E-BMD models.

Our second objective aimed to evaluate the short-term precision errors of HR-pQCT FE-derived failure load. For the STM approach, $CV\%_{RMS}$ ranged between 2.5% and 3.6%, which appeared to decrease by increasing the critical volume. For E-BMD with strain-based failure criteria, the precision error was ~5% and was not sensitive to critical volume. For E-BMD with stress-based failure criteria, the precision errors were smaller compared to the strain-based E-BMD model but were somewhat variable, ranging between 2.5% to 4.5%.

For the STM and stress-based E-BMD models, our reported precision errors appeared to be comparable to those of cadaveric ($CV\%_{RMS}$: 2.5%) [61], but slightly larger than *in vivo* studies ($CV\%_{RMS}$: 2.5% and 1.5% for males and females, respectively) [60]. One reason for this might be the sample size, as we calculated *in vivo* precision errors for 28 postmenopausal women, whereas MacNeil et al. [60] calculated precision errors for 15 males and 15 females separately. Importantly, with these sample sizes, our precision errors have an upper 90% confidence limit less than 30% (e.g., if the precision error was 3%, then we are 90% confident

that the true precision error is less than 3.9%) [59]. With the sample sizes used in MacNeil et al. [60], the reported precision errors have an upper 90% confidence limit of ~50% [59]. Also, higher precision errors found here may be due to the age of the participants. We studied precision errors for postmenopausal women while participants in previous work were adults with ages ranging from 20 to 40 [60]. Importantly, skeletal precision may vary based on the duration or time from menopause and osteoporosis status [56]. Moreover, as the results of a study by Paggiosi et al. suggested, older participants may have more difficulty remaining still, which can result in more motion artifact, more exclusion of scans, and less precision [75]. As a study by Kawalilak et al. [16] indicated that there is no significant difference between bone outcomes (i.e., density and structural) between postmenopausal women and young adults, this discrepancy between our work and MacNeil et al. [60] merits further investigation into population-specific precision errors of HR-pQCT based distal radius failure loads.

In order to recommend a failure criteria for use within future FE models, different parameters including explained variance (R^2), precision error ($CV\%_{RMS}$), time and effort required for analysis (including segmentation and FE analysis), and the ability to monitor changes in bone need to be considered, simultaneously. With regards to explained variance, our results indicated that STM and E-BMD with Pistoia's strain-based failure criteria and E-BMD with stress-based failure criteria (with a low critical volume of 0.1%) provide comparable predictions of forearm failure load. With regards to precision error, STM and E-BMD with stress-based failure criteria offered smaller precision errors than E-BMD with strain-based failure criteria. Also, for the critical volumes corresponding to higher R^2 values for each of STM or stress-based E-BMD models, precision errors were smaller for the STM model than the stress-based E-BMD model. With regards to time and effort, development time was comparable between the three approaches; however, the FE solving time with E-BMD was much longer (~3 hours for STM; ~5 hours for E-BMD). Finally, although the E-BMD model did not require segmentation of bone microstructure, which is sensitive to partial volume effects due the limited resolution of 82 µm, its predictions of failure load and precision errors were comparable to those of the STM model. All-in-all, these results indicate that the STM approach using Pistoia's criteria appears best suited for non-invasively predicting forearm failure load. However, if the aim of the research is to monitor changes in bone strength during growth and/or aging, or to quantify the effect of diseases and treatments which may influence on bone tissue mineralization or porosity, the E-BMD method may be best suited because this model can account for differences in tissue mineralization. In this case, we recommend using the E-BMD model with stress-based failure criteria with a critical volume of 0.1%.

A strength of this study was using intact forearms for mechanical testing simulating a fall on the extending forearm and hand, resulting in clinically comparable distal radius fractures [43]. A second strength pertained to the use of fresh-frozen cadaveric samples, which avoided mechanical property variation induced by embalming, as reported in several studies [44, 45, 66]. A third strength pertained to our *in vivo* study of postmenopausal women participants as well as *ex vivo* cadaver study with an age representative of postmenopausal women, a clinically relevant population at high risk of fracture. Finally, we had a sample size of 28 postmenopausal women for the estimation of precision errors, which met requirements set by Glüer et al., [59].

Limitations of this study pertained to the sample size of cadaveric forearms and experimental testing speed. First, our study was limited to 13 specimens of older female forearms for the experimental study. Although focusing on specimens from older women donors is clinically relevant, the results of this study cannot be generalized to populations with different age or sex. Also, due to the small sample size and small differences in the values of R^2 between the STM and E-BMD models, a statistical comparison between the values of R^2 is not possible as a larger sample size is required to detect such small differences. Second, we applied a slow testing rate (3mm/sec), which differs from dynamic rates experienced during a fall (> 1m/sec) [76]. However, it should be noted that similar rates have been used in other previous studies [12, 26, 29], and this testing protocol is shown to be successful in simulating distal radius fractures due to a fall [43].

4.5. Summary

In summary, HR-pQCT based FE models of distal radius bone sections explained high variance in the failure load of intact forearm under fall configuration testing ($R^2 \approx 0.90$) with precision errors less than 5%. The STM and E-BMD models with Pistoia's strain-based failure criteria (2% critical volume) and E-BMD with stress-based failure criteria (0.1% critical volume) provided comparable predictions of failure load from a fall configuration testing with *in vivo* precision errors ≤ 5%. Taking into account the comparable coefficient of determination, precision error, and time and effort required for analysis, we concluded that STM with the current strain-based failure criteria proposed by Pistoia provides acceptable predictions of forearm failure load. However, if the aim of the study is to monitor changes in bone caused by disease, treatment, or growth, which may affect tissue mineralization, the E-BMD method may be best suited. Accordingly, we recommend using the E-BMD model with stress-based failure criteria and critical volume of 0.1%. On a related note, caution is required when selecting

critical volume for the E-BMD model with the stress-based failure criteria, and critical volumes larger than 1% (e.g., via Pistoia's 2% volume) is not recommended.

Chapter 5 HR-pQCT based finite element models of the distal radius from the standard and anatomically standardized region do not differ and explain similar variance in experimentally-derived failure load

5.1. Introduction

The standard distal radius assessment with HR-pQCT consists of scanning a region of interest located 9.5mm proximal to the end plate [77]. Although using this standard fixed region of interest is a simple and repeatable process, it does not consider differences in densitometric and geometric variation across bone length [78, 79]. As such, the use of a fixed region of interest could introduce bias when bone strength is compared across individuals with different bone lengths (e.g., ethnicity and sex comparisons) [18]. Additionally, a fixed region of interest introduces uncertainty when comparing HR-pQCT-acquired forearm properties of an individual against a reference population if the individual's bone lengths differ from the population mean [18]. Accordingly, a protocol with scanning site (region of interest) based on relative bone length provides comparable anatomical site between individuals with different bone lengths [18].

Prior research evaluating explained variance in forearm failure load using HR-pQCT and FE utilized the fixed standard region [12, 15]. It is unclear if FE predictions acquired from the 4% region explain similar variance in forearm failure load.

Thus, our first objective was to compare FE-predictions of distal radius failure load acquired from the fixed region and the 4% region. Our second objective was to evaluate explained variance in experimentally-derived forearm failure load of fall configuration test acquired with HR-pQCT FE analyses of the fixed and the 4% regions.

5.2. Methods

5.2.1. Specimens

For Objective 1, we acquired forty (n = 40) female fresh-frozen cadaveric forearms from an anatomical tissue bank (mean age (SD): 81.7 (9.4) years). These specimens were from older women representing the population at higher risk of forearm fracture [70]. Specimens were extended from the finger-tip to mid-humerus. Sample preparation protocol was the same as Chapter 4 (Heading 4.2.1). We measured radius length from radial head to tip of radial styloid process using a ruler. For Objective 2, we used nineteen (n = 19) of the fresh-frozen cadavers (83.7 (8.3) years), same as in Chapter 4 (Heading 4.2.1).

5.2.2. HR-pQCT imaging

An experienced operator scanned each forearm twice using HR-pQCT (XtremeCT; Scanco Medical, Switzerland) with an isotropic voxel size of 82 µm (60 kV, 1 mA current, 200 ms integration time) according to our lab protocols [56]. Using the scout view image, the operator positioned the standard reference line on the anatomic landmark and scanned the standard 9.02 mm region of interest (110 parallel slices), located 9.5 mm proximal to the reference line [56]. Next, the operator scanned nine consecutive stacks of 110 slices starting from the standard reference line, which were used to identify the 4% region (discussed below). The scan duration was approximately 3 minutes and 25 minutes for the first and second scans, respectively. We calibrated all images using a manufacturer-provided phantom with known calcium hydroxyapatite (HA) equivalent concentrations.

5.2.3. HR-pQCT image analysis & FE analysis

We defined two regions of interest (ROI) including the fixed and 4% regions. The length of each ROI was 9.02 mm (110 slices with 82 µm voxel size). The operator located the first (fixed) region 9.5 mm proximal to the standard reference line [56]. The 4% region was defined from the 9-stack of consecutive scans. A trained operator (SH) used the "skier" protocol, as per Bonaretti et al. [18], to identify the reference line at the proximal margin of the radius endplate, with the 4% region defined relative to this line (Figure 0-1 (a)). We completed image analysis according to the manufacturer's recommendations for standard evaluation (Scanco Module 64-bit IPL V5.08b). Another trained operator (NS) segmented bone from surrounding tissue semi-automatically using a fixed global threshold of 400 mg HA/cm^3. The operator modified the automatically generated contour line. In terms of positioning, the 4% region was more distal than the fixed region in 38 of 40 specimens (95%). The fixed and 4% regions had an overlap ranging from 5.8 mm-9 mm. For each ROI, we performed FE analysis using the protocol explained in Chapter 4 (Heading 4.2.3) (Figure 0-1 (b)). For both models, we used Pistoia's failure criteria [12].

5.2.4. Mechanical testing

For this study, we used the data acquired from the mechanical testing explained in Chapter 4 (Heading 4.2.4) (Figure 0-1 (c)).

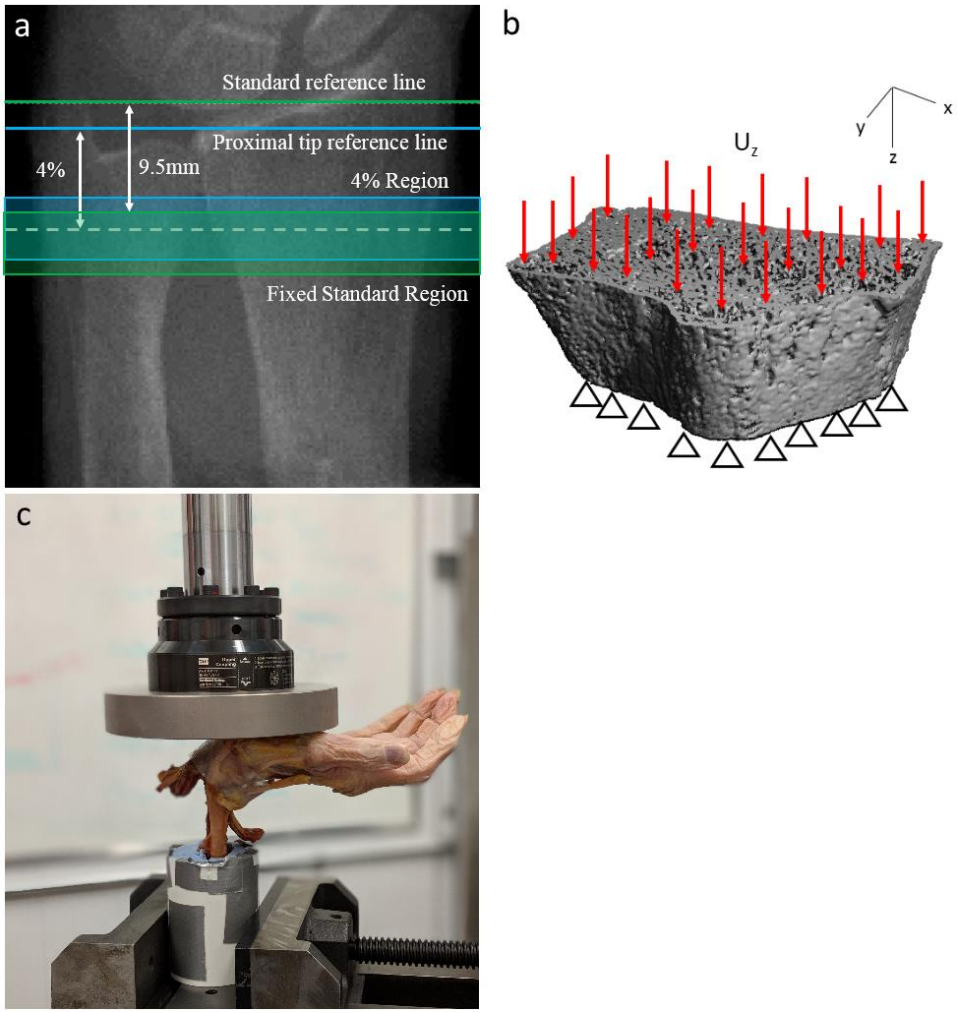

Figure 0-1 (a) Scout view image of radius indicating the standard reference line, proximal reference line, fixed region, and 4% region. The proximal tip reference line was identified using the "skier" approach [18]. The first slice of the fixed region is located at a constant distance of 9.5 mm from the standard reference line, while the distance of the center slice of the 4% region from the proximal reference line is proportional to bone length. (b) Indication of µFE model with boundary conditions. (c) Mechanical testing setup for uniaxial compression test on intact forearm.

5.2.5. Statistical analysis

We investigated the effect of region of interest (fixed vs 4%) on HR-pQCT derived bone failure load using a paired t-test (significance level $p<0.05$). For Objective 2, we used linear regression to assess relationships between experimentally-derived and FE-derived failure load for the two regions. Statistical analyses were performed using IBM SPSS statistics software (Version 24.0).

5.3. Results

The failure load from the 4% region did not differ significantly from the fixed region (p = 0.054). FE-derived failure load at the fixed region explained 89% variance in experimentally derived forearm failure load. Failure load acquired from the 4% region explained 87% variance in the experimental failure load.

Table 0-1 Mean and standard deviations of the HR-pQCT based FE-derived failure load for two regions (fixed vs 4%) at distal radius (N=40). Differences between the two (with respect to the fixed region) are given in absolute (with their 95% confidence intervals) and percentages of the fixed region values with significance tested using paired t-test.

Parameter	**Fixed region**	**4% region**	**Difference (units)**	**Difference (%)**	**95% CI** *Lower* *Upper*		**p-value**
Failure Load *(kN)*	2.97 ± 0.79	2.94 ± 0.77	-0.03	-0.93	-0.06	0.00	0.054

5.4. Discussion

The first objective of this study aimed to compare HR-pQCT based failure load of the distal radius bone sections obtained from the fixed and the anatomically standardized regions. No significant difference was observed between the means of failure loads derived from the two regions. One reason for this similarity could be that the two regions have considerable overlap (5.8 mm- 9 mm). This finding is in line with results obtained *in vivo* by Bonaretti et al. [18]. In our study, the average location of the middle slice of the fixed region and 4% regions are approximately 4.5% and 4% of radius length away from the proximal reference line, respectively. In their study, Bonaretti et al. [18] estimated the average percent offset of the fixed region from the proximal reference line for several studies [80–87], and showed that all of the offsets are approximately 4% ulna length away from the reference line. This might justify the similarity between the results of this study and those of Bonaretti et al. [18].

The second objective of this study was to evaluate FE-predictions of forearm failure load acquired from the fixed region and the 4% region in relation to experimental forearm failure load from fall configuration testing. Our results indicated that the fixed and 4% regions explained similar variance in experimental forearm failure load under fall configuration testing (i.e., with coefficients of determination of 0.89 and 0.87, respectively). This similarity of predictions was anticipated due to similarity of FE estimates of distal radius failure loads between the regions. It has been shown that both sites correspond with the location of forearm fracture (i.e., as a result of a fall onto outstretched hand) at the location of their overlap [37]. Based on our results, both regions can be used to estimate forearm failure load for a population similar to this study (i.e., postmenopausal women), without large variations in body size and limb length. However, in case of cross-sectional studies with large variations in sample limb length the fixed region might induce bias. Further, the results of this study indicated that HR-pQCT-based FE models of bone sections can be used to clinically predict fall configuration forearm failure load of postmenopausal women.

The coefficient of determination of this study appeared higher than that reported in the study of Pistoia et. al., [26] (89% vs 66%). This can be mainly due to using fresh-frozen specimens, while Pistoia et al used embalmed specimens, for which the mechanical properties may change [44, 66]. Further, the coefficient of determination of this study appeared higher than that reported in the study of Mueller et. al., [29] (89% vs 73%). This may also be because of including embalmed samples from both males and females in their study. The location of fracture might be different for males and females due to the difference in limb length, and the

fracture might not be inside the region of interest used for FE analysis. Also, the values of failure load might be different between males and females (i.e., likely the failure load for males is larger than females). As a result, including the failure loads from both males and females in a single regression analysis might have reduced the coefficient of determination of the regression.

The strengths of this study relate to our analysis of postmenopausal females prone to fracture, mechanical testing protocol, and use of fresh-frozen cadavers. First, our bone specimens included older women, representing clinically relevant population at high risk for bone fragility and fracture. Second, we used intact fresh-frozen female forearms with a mechanical testing setup successful in simulating forearm fracture from falling onto outstretched hand [43]. This test offers representative measures of forearm loading and failure load, whereas compression testing of excised radius samples may not simulate loading conditions experienced during a fall. Third, our use of fresh-frozen cadaveric samples avoided mechanical property variation induced by embalming [44, 45, 66].

Study limitations relate to a small sample size for regression analysis, reference line selection and limb length measurement. First, the second objective of this study was limited to 13 specimens with similar sizes, which could be a reason that we did not notice a difference in FE-derived failure load with the fixed versus 4% region. Accordingly, it would be useful to repeat this study with a greater range of specimen sizes including male donors. Second, we measured the length of the radius as a representative measure of limb length whereas Bonaretti et al. [18] measured the length of the ulna. Although this could lead to positional error, the difference between the position of the distal 4% region due to this error is comparable to the error associated with physically measuring the ulna or radius length [18]. Finally, we found that defining the position of the reference line using the "skier" approach was challenging, particularly for samples with blurry scout view images, which can lead to a measurement error. However, accurate reference line placement with the standard method was also somewhat challenging, with reference line positioning precision errors corresponding to 3.3% of total length of the region of interest (0.29 mm of 9.02 mm) according to Bonaretti et al. [88].

In conclusion, HR-pQCT derived failure load did not differ between the fixed region and 4% region at distal radius. Additionally, both regions explained 87-89% of variance in experimental failure load of intact forearms under a fall configuration test. Our results indicated that either region can be applied to non-invasively predict wrist strength during a fall for postmenopausal women.

Chapter 6 Discussion

6.1. Overview of findings

The current HR-pQCT based FE model has been used in many studies as a replacement for the conventional indices (e.g., BMD) to predict intact forearm strength. This model has moderately improved intact forearm strength predictions; however, this standard model has some limitations. This research sought to address these limitations in order to improve the prediction of forearm failure load acquired from HR-pQCT FE models.

We proposed the following approaches to improve intact forearm strength predictions derived from HR-pQCT based FE models: addition of material property variation, evaluation of different failure criteria, and different scanning regions.

The main achievement of Chapter 4 (effect of failure criteria) was to show the effect of failure criteria on forearm failure load predictions and their precision error using different HR-pQCT based FE models. Failure criteria plays an important role in such models due to their linear nature. We found that the STM and the strain-based E-BMD models are not sensitive to the failure criteria, while the stress-based E-BMD model showed substantial changes with failure criteria. Further, STM and E-BMD models with Pistoia's strain-based failure criteria and E-BMD with stress-based failure criteria (with a critical volume of 0.1%) provided comparable predictions of forearm failure load with low precision errors. Taking into account the comparable coefficient of determination, precision error, time and effort required for analysis, we concluded that STM with the current strain-based failure criteria proposed by Pistoia provides acceptable predictions of forearm failure load. However, the use of E-BMD with stress-based failure criteria (critical volume of 0.1%) may be beneficial for monitoring changes in bone. Another achievement of this chapter is to provide evidence that HR-pQCT based FE models of distal radius bone sections may be clinically useful to predict wrist strength in postmenopausal women.

The main outcome of Chapter 5 was that using an anatomically standardized region of interest does not significantly change the HR-pQCT-based FE predictions of forearm failure load. More specifically, HR-pQCT-derived failure load was similar (i.e., no significant difference) for the fixed region and 4% region at distal radius. Additionally, both regions explained similar variance in experimentally-derived forearm failure load. Accordingly, both regions can be used to predict wrist strength. However, different results may be observed by using a sample set with large variations in body size and limb length, which requires further investigation.

6.2. Contributions

There are various contributions arising from this research worthy of mention. Firstly, this study provided evidence for the importance of failure criteria on wrist strength predictions when using HR-pQCT based FE models. We found that the STM and the strain-based E-BMD models were not affected by changing the critical volume (failed tissue percentage), whereas the stress-based E-BMD model was highly sensitive. Based on our findings, we provided further evidence that both STM and E-BMD models are suitable to predict fall configuration forearm failure load. Further, our results indicated that HR-pQCT FE models of distal radius sections can explain 87-89% of variance in failure load of intact forearm under fall configuration testing (i.e., compression on outstretched hand which is shown to replicate distal radius fracture due to fall [43]). Finally, for the first time in the literature, we estimated precision errors for failure load predictions using different models and failure criteria and showed that precision errors were less than 5%.

Moreover, we showed that without a wide range of body or limb size, the failure load of the fixed and anatomically standardized regions did not significantly differ. Further, both regions provided similar prediction of fall configuration forearm failure load (0.89 and 0.87, respectively).

6.3. Clinical significance

These findings provided further evidence that HR-pQCT FE models of distal radius can be used to predict bone strength on the extended forearm after a fall in older women. This could also be combined with predictions for impact load placed on the radius during a forward fall (based on height, weight and sex) in order to assess the fracture risk (via a safety factor) of patients. The E-BMD model may also be useful to monitor changes in bone mechanical properties and bone mineralization. For example, changes in bone failure load due to growth, diseases, different activities, nutrition or medication.

Ultimately, this tool may improve human health by identifying individuals at risk of wrist fracture. Also, it may be an attractive tool to predict risk of other osteoporotic fractures such as hip or spine for individuals with wrist fracture.

6.4. Future work

- Related to one of the limitations of the current study, future work can focus on correlating FE-derived failure load and experimentally-measured failure load of the intact forearm using more samples. Moreover, using different sample sets including different age and sex groups can be studied in future research. This can be helpful to generalize the results of this study to a broader population.
- Further, future studies can focus on performing mechanical testing at higher speeds. Although the current protocol has been successful in replicating distal radius fractures due to falling [43], it might be beneficial to perform testing at higher speeds.
- In addition to the approach presented in this research, we have proposed other approaches which may help to improve HR-pQCT-based predictions of forearm failure load, as follows:
    - Inclusion of ulna: the standard model does not include the ulna in FE model. Also, it is not known how much of the load applied to the forearm during a fall is carried by the ulna. Hence, measuring the load applied to the ulna during fall configuration testing and accounting for the ulna in FE models may improve forearm strength predictions.
    - Density-based failure criteria: The current HR-pQCT-based FE model, which is used in the current study, uses a fixed threshold for failure strain and stress. However, for the E-BMD model, a fixed stress threshold might not be ideal due to the varying elastic modulus of elements. Thus, using a critical stress value based on element density may improve the forearm predictions of the stress-based E-BMD model.
    - Off-axis loading: It is known that the forearm does not undergo pure axial loading during a fall. The major components of a load applied to a forearm are axial loading as well as bending. However, the current HR-pQCT FE model only simulates pure axial loading. Therefore, applying a more realistic boundary condition might improve forearm failure load predictions. This can be achieved by applying an off-axis load, which simulates both axial compression and bending.

REFERENCES

1. Engelke K, van Rietbergen B, Zysset P. FEA to Measure Bone Strength: A Review. Clin Rev Bone Miner Metab. 2016;14:26–37.

2. Consensus development conference: Diagnosis, prophylaxis, and treatment of osteoporosis. Am J Med. 1993;94:646–50.

3. Consensus development conference: Diagnosis, prophylaxis, and treatment of osteoporosis. Am J Med. 1991;90:107–10.

4. Leslie WD, Morin SN. Osteoporosis epidemiology 2013: implications for diagnosis, risk assessment, and treatment. Curr Opin Rheumatol. 2014;26:440–6. doi:10.1097/BOR.0000000000000064.

5. Papaioannou A, Morin S, Cheung AM, Atkinson S, Brown JP, Feldman S, et al. 2010 clinical practice guidelines for the diagnosis and management of osteoporosis in Canada: Summary. CMAJ. 2010;182:1864–73.

6. Cuddihy MT, Gabriel SE, Crowson CS, O'Fallon WM, Melton LJ. Forearm fractures as predictors of subsequent osteoporotic fractures. Osteoporos Int. 1999;9:469–75.

7. Järvinen TLN, Sievänen H, Khan KM, Heinonen A, Kannus P. Shifting the focus in fracture prevention from osteoporosis to falls. Br Med J. 2008;336:124–6. http://pubmedcentralcanada.ca/picrender.cgi?accid=PMC2206310&blobtype=pdf.

8. Mallmin H, Ljunghall S, Persson I, Naessén T, Krusemo UB, Bergström R. Fracture of the distal forearm as a forecaster of subsequent hip fracture: a population-based cohort study with 24 years of follow-up. Calcif Tissue Int. 1993;52:269–72. http://www.ncbi.nlm.nih.gov/pubmed/8467406.

9. Peel NFA, Barrington NA, Smith TWD, Eastell R. Distal forearm fracture as risk factor for vertebral osteoporosis. BMJ. 1994;308:1543–4.

10. Riggs BL, Melton LJ, Robb RA, Camp JJ, Atkinson EJ, Oberg AL, et al. Population-Based Analysis of the Relationship of Whole Bone Strength Indices and Fall-Related Loads to Age- and Sex-Specific Patterns of Hip and Wrist Fractures. J bone Miner Res. 2006;21:315–23.

11. Gay J. Radial fracture as an indicator of osteoporosis : Can Med Assoc J. 1974;111:156–157.

12. Pistoia W, van Rietbergen B, Lochmüller E-M, Lill CA, Eckstein F, Rüegsegger P. Estimation of distal radius failure load with micro-finite element analysis models based on three-dimensional peripheral quantitative computed tomography images. Bone. 2002;30:842–8.

13. Stone KL, Seeley DG, Lui L, Cauley J a, Ensrud KE, Browner WS, et al. BMD at multiple sites and risk of fracture of multiple types: long-term results from the Study of Osteoporotic Fractures. J Bone Miner Res. 2003;18:1947–54. doi:10.1359/jbmr.2003.18.11.1947.

14. Siris ES, Miller PD, Barrett-Connor E, Faulkner KG, Wehren LE, Abbott TA, et al. Identification and fracture outcomes of undiagnosed low bone mineral density in postmenopausal women: results from the National Osteoporosis Risk Assessment. JAMA. 2001;286:2815–22. doi:10.1001/jama.286.22.2815.

15. van Rietbergen B, Ito K. A survey of micro-finite element analysis for clinical assessment of bone strength: The first decade. J Biomech. 2015;48:832–41. doi:10.1016/j.jbiomech.2014.12.024.

16. Kawalilak CE, Johnston JD, Olszynski WP, Leswick DA, Kontulainen SA. Precision and Quality Assurance Issues Comparison of Short-Term In Vivo Precision of Bone Density and Microarchitecture at the Distal Radius and Tibia Between Postmenopausal Women and Young Adults. J Clin Densitom. 2014;17:510–7. doi:10.1016/j.jocd.2013.09.014.

17. Shanbhogue V V., Hansen S, Halekoh U, Brixen K. Use of relative vs fixed offset distance to define region of interest at the distal radius and tibia in high-resolution peripheral quantitative computed tomography. J Clin Densitom. 2015;18:217–25. doi:10.1016/j.jocd.2014.12.002.

18. Bonaretti S, Majumdar S, Lang TF, Khosla S, Burghardt AJ. The comparability of HR-pQCT bone measurements is improved by scanning anatomically standardized regions. Osteoporos Int. 2017;:1–14.

19. Drake RL, Vogl AW, Mitchell AWM. Gray's Anatomy for Students, Second Edition. 2010.

20. Rho JY, Kuhn-Spearing L, Zioupos P. Mechanical properties and the hierarchical structure of bone. Med Eng Phys. 1998;20:92–102.

21. Keaveny TM, Morgan EF, Yeh OC. Bone Mechanics. Stand Handb Biomed Eng Des. 2004;:8.1-8.23.

22. Kingston B. Understanding Joints: A Practical Guide to Their Structure and Function. 2000.

23. Kaplan EB. Kaplan's functional and surgical anatomy of the hand. 3rd edition. Lippincott Williams & Wilkins; 1984.

24. Goldfarb C a, Yin Y, Gilula L a, Fisher a J, Boyer MI. Wrist fractures: what the clinician wants to know. Radiology. 2001;219:11–28.

25. Melton LJ, Christen D, Riggs BL, Achenbach SJ, Müller R, Van Lenthe GH, et al. Assessing forearm fracture risk in postmenopausal women. Osteoporos Int. 2010;21:1161–9.

26. Pistoia W, van Rietbergen B, Lochmüller E-M, Lill CA, Eckstein F, Rüegsegger P. Image-based micro-finite-element modeling for improved distal radius strength diagnosis: moving from bench to bedside. J Clin Densitom. 2004;7:153–60.

27. MacNeil JA, Boyd SK. Bone strength at the distal radius can be estimated from high-resolution peripheral quantitative computed tomography and the finite element method. Bone. 2008;42:1203–13.

28. Varga P, Pahr DH, Baumbach S, Zysset PK. HR-pQCT based FE analysis of the most distal radius section provides an improved prediction of Colles' fracture load in vitro. Bone. 2010;47:982–8. doi:10.1016/j.bone.2010.08.002.

29. Mueller TL, Christen D, Sandercott S, Boyd SK, van Rietbergen B, Eckstein F, et al. Computational finite element bone mechanics accurately predicts mechanical competence in the human radius of an elderly population. Bone. 2011;48:1232–8.

30. Blake GM, Fogelman I. The role of DXA bone density scans in the diagnosis and treatment of osteoporosis. Postgraduate Medical Journal. 2007;83:509–17.

31. Kanis JA, Kanis JA. Assessment of fracture risk and its application to screening for postmenopausal osteoporosis: Synopsis of a WHO report. Osteoporos Int. 1994;4:368–81.

32. van Rietbergen B, Weinans H, Huiskes R, Odgaard A. A new method to determine trabecular bone elastic properties and loading using micromechanical finite-element models. J Biomech. 1995;28:69–81.

33. Hansen S, Brixen K, Gravholt CH. Compromised trabecular microarchitecture and lower finite element estimates of radius and tibia bone strength in adults with turner syndrome: A cross-sectional study using high-resolution-pQCT. J Bone Miner Res. 2012;27:1794–803.

34. Burghardt AJ, Kazakia GJ, Sode M, De Papp AE, Link TM, Majumdar S. A longitudinal HR-pQCT study of alendronate treatment in postmenopausal women with low bone density: Relations among density, cortical and trabecular microarchitecture, biomechanics, and bone turnover. J Bone Miner Res. 2010;25:2282–95.

35. Chevalley T, Bonjour JP, Van Rietbergen B, Rizzoli R, Ferrari S. Fractures in healthy females followed from childhood to early adulthood are associated with later menarcheal age and with impaired bone microstructure at peak bone mass. J Clin Endocrinol Metab. 2012;97:4174–81.

36. Schipilow JD, Macdonald HM, Liphardt AM, Kan M, Boyd SK. Bone micro-architecture, estimated bone strength, and the muscle-bone interaction in elite athletes: An HR-pQCT study. Bone. 2013;56:281–9.

37. Eastell R, Wahner HW, O'Fallon M, Amadio PC, Melton LJ, Riggs BL. Unequal decrease in bone density of lumbar spine and ultradistal radius in Colles' and vertebral fracture syndromes. J Clin Invest. 1989;83:168–74.

38. Eckstein F, Lochmüller E-M, Lill C a, Kuhn V, Schneider E, Delling G, et al. Bone strength at clinically relevant sites displays substantial heterogeneity and is best predicted from site-specific bone densitometry. J Bone Miner Res. 2002;17:162–71.

39. Augat P, Iida H, Jiang Y, Diao E, Genant HK. Distal radius fractures: Mechanisms of injury and strength prediction by bone mineral assessment. J Orthop Res. 1998;16:629–35.

40. Varga P, Dall'Ara E, Pahr DH, Pretterklieber M, Zysset PK. Validation of an HR-pQCT-based homogenized finite element approach using mechanical testing of ultra-distal radius sections. Biomech Model Mechanobiol. 2011;10:431–44.

41. Zhou B, Wang J, Yu YE, Zhang Z, Nawathe S, Nishiyama KK, et al. High-resolution peripheral quantitative computed tomography (HR-pQCT) can assess microstructural and biomechanical properties of both human distal radius and tibia: Ex vivo computational and experimental validations. Bone. 2016;86:58–67. doi:10.1016/j.bone.2016.02.016.

42. Hosseini HS, Dünki A, Fabech J, Stauber M, Vilayphiou N, Pahr D, et al. Fast estimation of Colles' fracture load of the distal section of the radius by homogenized finite element analysis based on HR-pQCT. Bone. 2017;97:65–75. doi:10.1016/j.bone.2017.01.003.

43. Wagner DW, Lindsey DP, Beaupre GS. Replicating a Colles fracture in an excised radius:

Revisiting testing protocols. J Biomech. 2012;45:997–1002. doi:10.1016/j.jbiomech.2012.01.014.

44. Öhman C, Dall'Ara E, Baleani M, Jan SVS, Viceconti M. The effects of embalming using a 4% formalin solution on the compressive mechanical properties of human cortical bone. Clin Biomech. 2008;23:1294–8.

45. McElhaney J, Fogle J, Byars E, Weaver G. Effect of embalming on the mechanical properties of beef bone. J Appl Physiol. 1964;19:1234–6. http://jap.physiology.org/content/19/6/1234.

46. Lochmüller EM, Lill CA, Kuhn V, Schneider E, Eckstein F. Radius Bone Strength in Bending, Compression, and Falling and Its Correlation With Clinical Densitometry at Multiple Sites. J Bone Miner Res. 2002;17:1629–38.

47. Iwamoto K, Hamanaka Y, Yamamoto I, Niiho C. Correlation between the values of bone measurements using DXA, QCT and USD methods and the bone strength in calcanei in vivo. Acta Anat Nippon. 1998;73:509–15.

48. Baum T, Kutscher M, Müller D, Räth C, Eckstein F, Lochmüller EM, et al. Cortical and trabecular bone structure analysis at the distal radius-prediction of biomechanical strength by DXA and MRI. J Bone Miner Metab. 2013;31:212–21.

49. Hudelmaier M, Kuhn V, Lochmüller EM, Well H, Priemel M, Link TM, et al. Can geometry-based parameters from pQCT and material parameters from quantitative ultrasound (QUS) improve the prediction of radial bone strength over that by bone mass (DXA)? Osteoporos Int. 2004;15:375–81.

50. Muller ME, Webber CE, Bouxsein ML. Predicting the failure load of the distal radius. Osteoporos Int. 2003;14:345–52.

51. Hosseinitabatabaei S, Ashjaee N, Tahani M. Introduction of Maximum Stress Parameter for the Evaluation of Stress Shielding around Orthopedic Screws in the Presence of Bone Remodeling Process. J Med Biol Eng. 2016.

52. Amini M, Nazemi SM, Lanovaz JL, Kontulainen S, Masri BA, Wilson DR, et al. Individual and combined effects of OA-related subchondral bone alterations on proximal tibial surface stiffness: A parametric finite element modeling study. Med Eng Phys. 2015;37:783–91. doi:10.1016/j.medengphy.2015.05.011.

53. Gefen A. Computational simulations of stress shielding and bone resorption around existing and computer-designed orthopaedic screws. Med Biol Eng Comput. 2002;40:311–22.

54. Boutroy S, Van Rietbergen B, Sornay-Rendu E, Munoz F, Bouxsein ML, Delmas PD. Finite element analysis based on in vivo HR-pQCT images of the distal radius is associated with wrist fracture in postmenopausal women. J Bone Miner Res. 2008;23:392–9.

55. Vilayphiou N, Boutroy S, Sornay-rendu E, Munoz F, Delmas PD, Chapurlat R, et al. Finite element analysis performed on radius and tibia HR-pQCT images and fragility fractures at all sites in postmenopausal women. Bone. 2010;46:1030–7.

56. Kawalilak CE, Kontulainen SA, Amini MA, Lanovaz JL, Olszynski WP, Johnston JD. In vivo precision of three HR-pQCT-derived finite element models of the distal radius and tibia in postmenopausal women. BMC Musculoskelet Disord. 2016;17:389. doi:10.1186/s12891-016-1238-x.

57. Niebur GL, Feldstein MJ, Yuen JC, Chen TJ, Keaveny TM. High-resolution finite element models with tissue strength asymmetry accurately predict failure of trabecular bone. J Biomech. 2000;33:1575–83.

58. Verhulp E, Van Rietbergen B, Muller R, Huiskes R. Micro-finite element simulation of trabecular-bone post-yield behaviour--effects of material model, element size and type. Comput Methods Biomech Biomed Engin. 2008;11:389–95.

59. Glüer CC, Blake G, Lu Y, Blunt1 BA, Jergas1 M, Genant1 HK. Accurate assessment of precision errors: How to measure the reproducibility of bone densitometry techniques. Osteoporos Int. 1995;5:262–70.

60. MacNeil JA, Boyd SK. Improved reproducibility of high-resolution peripheral quantitative computed tomography for measurement of bone quality. Med Eng Phys. 2008;30:792–9.

61. Mueller TL, Stauber M, Kohler T, Eckstein F, Müller R, van Lenthe GH. Non-invasive bone competence analysis by high-resolution pQCT: An in vitro reproducibility study on structural and mechanical properties at the human radius. Bone. 2009;44:364–71.

62. Duckham RL, Frank AW, Johnston JD, Olszynski WP, Kontulainen SA. Monitoring time interval for pQCT-derived bone outcomes in postmenopausal women. Osteoporos Int. 2013;24:1917–22.

63. Engelke K, Adams JE, Armbrecht G, Augat P, Bogado CE, Bouxsein ML, et al. Clinical

Use of Quantitative Computed Tomography and Peripheral Quantitative Computed Tomography in the Management of Osteoporosis in Adults: The 2007 ISCD Official Positions. J Clin Densitom. 2008;11:123–62.

64. Burrows M, Liu D, Perdios A, Moore S, Mulpuri K, McKay H. Assessing bone microstructure at the distal radius in children and adolescents using HR-pQCT: A methodological pilot study. J Clin Densitom. 2010;13:451–5. doi:10.1016/j.jocd.2010.02.003.

65. Kawalilak CE, Bunyamin AT, Björkman KM, Johnston JD, Kontulainen SA. Precision of bone density and micro-architectural properties at the distal radius and tibia in children: an HR-pQCT study. Osteoporos Int. 2017;28:3189–97.

66. Burkhart KJ, Nowak TE, Blum J, Kuhn S, Welker M, Sternstein W, et al. Influence of formalin fixation on the biomechanical properties of human diaphyseal bone. In: Biomedizinische Technik. 2010. p. 361–5.

67. Roschger P, Paschalis EP, Fratzl P, Klaushofer K. Bone mineralization density distribution in health and disease. Bone. 2008;42:456–66.

68. Ruffoni D, Fratzl P, Roschger P, Klaushofer K, Weinkamer R. The bone mineralization density distribution as a fingerprint of the mineralization process. Bone. 2007;40:1308–19.

69. Homminga J, Huiskes R, Van Rietbergen B, Rüegsegger P, Weinans H. Introduction and evaluation of a gray-value voxel conversion technique. J Biomech. 2001;34:513–7.

70. Mueller TL, van Lenthe GH, Stauber M, Gratzke C, Eckstein F, Müller R. Regional, age and gender differences in architectural measures of bone quality and their correlation to bone mechanical competence in the human radius of an elderly population. Bone. 2009;45:882–91.

71. Owen RA, Melton LJ, Johnson KA, Ilstrup DM, Riggs BL. Incidence of Colles' fracture in a North American community. Am J Public Health. 1982;72:605–7.

72. Edwards WB, Troy KL. Finite element prediction of surface strain and fracture strength at the distal radius. Med Eng Phys. 2012;34:290–8. doi:10.1016/j.medengphy.2011.07.016.

73. Rousseeuw PJ, van Zomeren BC. Unmasking multivaraite outliers and leverage points. J Am Stat Assoc. 1990;85:633–639 ST–Unmasking multivaraite outliers and.

74. N.I.S.T/Sematech. Critical Values of the Chi-Square Distribution. E-handb Stat Methods. 2013;:1–4. doi:10.1016/B978-0-12-370502-0.50019-9.

75. Paggiosi MA, Eastell R, Walsh JS. Precision of high-resolution peripheral quantitative computed tomography measurement variables: Influence of gender, examination site, and age. Calcif Tissue Int. 2014;94:191–201.

76. Burkhart TA, Quenneville CE, Dunning CE, Andrews DM. Development and validation of a distal radius finite element model to simulate impact loading indicative of a forward fall. Proc Inst Mech Eng Part H J Eng Med. 2014;228:258–71.

77. Kawalilak CE, Johnston JD, Olszynski WP, Kontulainen SA. Characterizing microarchitectural changes at the distal radius and tibia in postmenopausal women using HR-pQCT. Osteoporos Int. 2014;25:2057–66.

78. Boyd SK. Site-Specific Variation of Bone Micro-Architecture in the Distal Radius and Tibia. J Clin Densitom. 2008;11:424–30.

79. Laib A, Häuselmann HJ, Rüegsegger P. In vivo high resolution 3D-QCT of the human forearm. Technol Health Care. 1998;6:329–37.

80. Szulc P, Boutroy S, Vilayphiou N, Chaitou A, Delmas PD, Chapurlat R. Cross-sectional analysis of the association between fragility fractures and bone microarchitecture in older men: the STRAMBO study. J bone Miner Res. 2011;26:1358–67.

81. Nilsson M, Sundh D, Ohlsson C, Karlsson M, Mellström D, Lorentzon M. Exercise during growth and young adulthood is independently associated with cortical bone size and strength in old Swedish men. J Bone Miner Res. 2014;29:1795–804.

82. Macdonald HM, Nishiyama KK, Kang J, Hanley DA, Boyd SK. Age-related patterns of trabecular and cortical bone loss differ between sexes and skeletal sites: a population-based HR-pQCT study. J Bone Miner Res. 2011;26:50–62.

83. Hung VWY, Zhu TY, Cheung W-H, Fong T-N, Yu FWP, Hung L-K, et al. Age-related differences in volumetric bone mineral density, microarchitecture, and bone strength of distal radius and tibia in Chinese women: a high-resolution pQCT reference database study. Osteoporos Int. 2015;26:1691–703.

84. Hansen S, Shanbhogue V, Folkestad L, Nielsen MMF, Brixen K. Bone microarchitecture and estimated strength in 499 adult Danish women and men: a cross-sectional, population-based high-resolution peripheral quantitative computed tomographic study on peak bone structure. Calcif Tissue Int. 2014;94:269–81.

85. Burghardt AJ, Kazakia GJ, Ramachandran S, Link TM, Majumdar S. Age-and gender-related differences in the geometric properties and biomechanical significance of intracortical porosity in the distal radius and tibia. J Bone Miner Res. 2010;25:983–93.

86. Boutroy S, Walker MD, Liu XS, McMahon DJ, Liu G, Guo XE, et al. Lower cortical porosity and higher tissue mineral density in Chinese American versus white women. J Bone Miner Res. 2014;29:551–61.

87. Wang Q, Wang X-F, Iuliano-Burns S, Ghasem-Zadeh A, Zebaze R, Seeman E. Rapid growth produces transient cortical weakness: a risk factor for metaphyseal fractures during puberty. J Bone Miner Res. 2010;25:1521–6.

88. Bonaretti S, Vilayphiou N, Chan CM, Yu A, Nishiyama K, Liu D, et al. Operator variability in scan positioning is a major component of HR-pQCT precision error and is reduced by standardized training. Osteoporos Int. 2017;28:245–57.

Appendix: Mechanical definitions

Similar to a spring, applying a load (e.g., force) to an object such as bone causes a displacement. By recording the values of force and displacement over time, the force-displacement curve can be obtained. The slope of the initial linear part of this curve is known as stiffness. Strain energy is the energy stored in material due to deformation, which is also the area under the force-displacement curve. The mentioned properties are known as structural properties, which depend on the object's size. On the other hand, these properties can be normalized to remove the effect of size. The resultant properties are known as material properties, which are discussed below (Figure A. 1).

Strain is defined as the ratio of change in length to the original length. Strain is dimensionless and can be measured physically. Stress is calculated by dividing the force acting on an area by the area. In the case of a linear elastic material, the ratio between stress and strain is known as Young's modulus or the elastic modulus (Figure A. 2).

Strain energy per unit volume is known as strain energy density, which can be calculated by dividing the strain energy by volume. Strain energy density is also the area under stress-strain curve. The strength of a material is its ability to withstand the applied loads or stresses. Poisson's ratio is defined as the ratio of transverse to longitudinal strains of a loaded specimen.

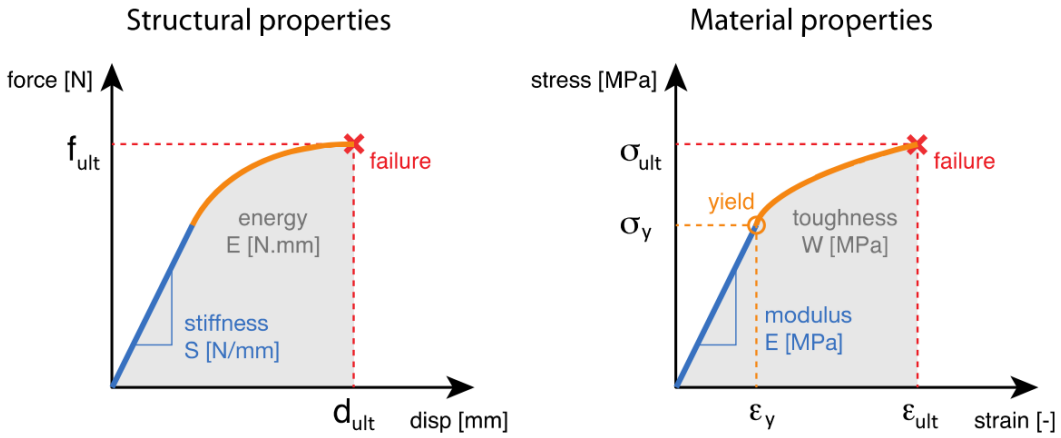

Figure A. 1. Comparison of structural and material properties. In contrast to the structural properties which depend on size, material properties normalize displacements by length into strains, forces by area into stresses and energy by volume into energy density. Material properties are required inputs for finite element analysis, while the structural properties are the principal outcome variables, (Image from Engelke et. al. [1]).

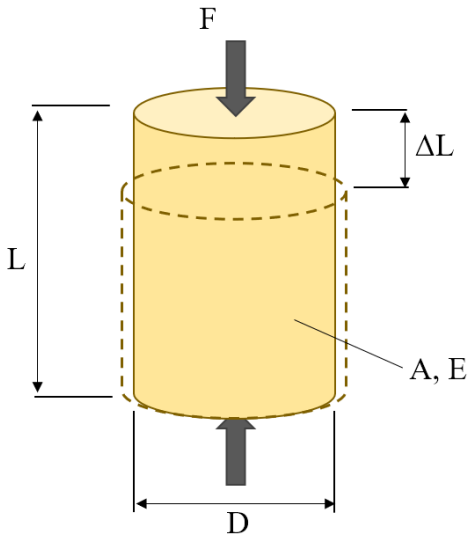

$$\text{stress}: \sigma_L = \frac{F}{A} \text{ [N/mm}^2 \textit{or} \text{ MPa]}$$

$$\text{strain}: \varepsilon_L = \frac{\Delta L}{L} \text{ [-]}$$

$$\varepsilon_R = \frac{\Delta D}{D} \text{ [-]}$$

$$\text{Young's modulus}: E = \frac{\sigma_L}{\varepsilon_L} \text{ [MPa]}$$

$$\text{Poisson's ratio}: \nu = \frac{\varepsilon_R}{\varepsilon_L}$$

Figure A. 2. Schematic illustration of mechanical definitions. L is the initial length of the cylinder. ΔL is the change in length of the cylinder due to compressive load of F. A is the cross-sectional area of the cylinder which can be calculated from the diameter D. E is the Young's modulus of the material, from which the cylinder is made.